Simulations of Magnetorotational Turbulence with a Higher-Order Godunov Scheme

Jacob B. Simon, John F. Hawley, Kris Beckwith

Department of Astronomy
University of Virginia
P.O. Box 400325
Charlottesville, VA 22904-4325

ABSTRACT

We apply a new, second-order Godunov code, Athena, to studies of the magnetorotational instability (MRI) using unstratified shearing box simulations with a uniform net vertical field and a sinusoidally varying zero net vertical field. The Athena results agree well with similar studies that used different numerical algorithms, including the observation that the turbulent energy decreases with increasing resolution in the zero net field model. We conduct analyses to study the flow of energy from differential rotation to turbulent fluctuations to thermalization. A study of the time-correlation between the rates of change of different volume-averaged energy components shows that energy injected into turbulent fluctuations dissipates on a timescale of Ω^{-1}, where Ω is the orbital frequency of the local domain. Magnetic dissipation dominates over kinetic dissipation, although not by as great a factor as the ratio of magnetic to kinetic energy. We Fourier-transform the magnetic and kinetic energy evolution equations and, using the assumption that the time-averaged energies are constant, determine the level of numerical dissipation as a function of length scale and resolution. By modeling numerical dissipation as if it were physical in origin, we characterize numerical resistivity and viscosity in terms of effective Reynolds and Prandtl numbers. The resulting effective magnetic Prandtl number is ~ 2, independent of resolution or initial field geometry. MRI simulations with effective Reynolds and Prandtl numbers determined by numerical dissipation are not equivalent to those where these numbers are set by physical resistivity and viscosity. These results serve, then, as a baseline for future shearing box studies where dissipation is controlled by the inclusion of explicit viscosity and resistivity.

Subject headings: Black holes - magnetohydrodynamics - stars:accretion

1. Introduction

The process of accretion powers a wide range of astrophysical systems, from protostars to quasars. In accretion disks, gravitational energy is converted into other forms including bulk outflows, heat, and radiation. In the traditional time-stationary thin disk model of Shakura & Syunyaev (1973), the r, ϕ component of the stress, $\tau_{r\phi}$, is proportional to the local pressure, $\tau_{r\phi} = \alpha P$. The α model assumes that the accretion energy is deposited as heat locally and radiated rapidly, providing a relation between disk emissivity and accretion rate. While the α model has proven valuable in interpreting many aspects of accretion systems, advancing beyond it will require a more detailed understanding of the stress that produces angular momentum transport as well as the physical processes involved in the subsequent thermalization and radiation of the orbital energy released by those stresses.

It is now understood that magnetohydrodynamic (MHD) turbulence generated by the magnetorotational instability (MRI) (Balbus & Hawley 1991, 1998) produces significant Maxwell stresses, $-B_r B_\phi/4\pi$, and Reynolds stresses, $\rho\delta v_r \delta v_\phi$, that account for transport within accretion disks. The absence of an analytic theory for MHD turbulence, however, means that direct numerical simulations play an essential role in investigating accretion physics. In this regard, local simulations, which reduce the problem to the simplest form that can sustain MRI-driven turbulence, have proven very useful. The "shearing box" model is a representation of a small patch of the disk constructed by boosting to a local co-rotating Cartesian frame that ignores geometric curvature but retains all rotational forces. MRI shearing box simulations were introduced by Hawley et al. (1995) and have been extensively used since then both without (e.g., Hawley et al. 1996; Balbus & Hawley 1998) and with vertical stratification (e.g., Brandenburg et al. 1995; Stone et al. 1996; Hirose et al. 2006).

Shearing box simulations can investigate several key questions including the functional dependence of the stress on disk properties and the turbulent energy flow that leads to dissipation as heat. These simulations have made it increasingly clear, for example, that the basic α stress parameterization is not only too simplistic, it is actually misleading. Shearing boxes have provided ample evidence that stress is *not* determined by pressure, at least in the usual manner of the α disk (Hawley et al. 1995; Sano et al. 2004). Early studies showed instead that stress is (in some cases) proportional to the *magnetic* pressure, but the magnetic energy is not itself directly determined by the gas and radiation pressure. Blackman et al. (2008) recently reviewed a large number of shearing box results and found that this result holds across the full ensemble of simulations with only small differences in the constant of proportionality from one run to another. The implications of these results are significant. For example, recent local simulations using stratified shearing boxes and radiation transport (Blaes et al. 2007; Krolik et al. 2007) have found no evidence of the thermal instability long

believed to be present in radiation-pressure supported α disks.

If stress is proportional to magnetic rather than total pressure, what determines the magnetic pressure in a disk? Apart from the expectation that the field will remain subthermal, this remains uncertain. The simplest shearing box simulations using ideal MHD have a limited range of significant parameters; this is both a strength and a weakness of that model. The magnetic energy in the saturated state could depend upon such factors as box size, the amplitude and geometry of the imposed initial magnetic field, and the ratio of the gas pressure to magnetic pressure (the plasma β value). Hawley et al. (1995) and Hawley et al. (1996) studied the effect of initial magnetic field topology on the resulting stress and found that although the MRI leads to turbulence regardless of the initial field, simulations that had an imposed net vertical field produce higher turbulence levels than an imposed toroidal field or a simulation that began with zero net magnetic flux within the domain. Hawley et al. (1995) found that the total magnetic energy and the resulting stress in the saturated turbulent state was a function of the initial plasma β with a uniform vertical field, namely that larger β (i.e., weaker fields) leads to smaller saturation levels. Other initial field configurations do not yield so direct a correlation between background field strength and saturation. Many simulations have failed to find any noticeable correlation between mean turbulent magnetic energy and the gas pressure. A comprehensive parameter study by Sano et al. (2004) observed at best only a very weak gas pressure dependence.

Since the mean magnetic energy at saturation is presumably a balance between continued driving by the MRI and loss due to magnetic dissipation and reconnection, there has been interest in going beyond ideal MHD to include explicit physical dissipation in the form of kinematic viscosity, ν, and Ohmic resistivity, η. Both of these properties have been shown to be important in determining the mean energies and stresses in MRI turbulence. Simulations by Hawley et al. (1996), Sano et al. (1998), Fleming et al. (2000), Sano & Inutsuka (2001), Ziegler & Rüdiger (2001), and Sano & Stone (2002) have investigated the impact of a nonzero η. The main result of these studies is that increasing the resistivity leads to a decrease in turbulence, independent of the initial field configuration. In zero net field models, the effect of resistivity on the turbulence is larger than one might expect from the linear MRI relation (Fleming et al. 2000). On the other hand, Hawley et al. (1996) found that increasing the viscosity increased the magnetic energy in the saturated state. Recent work has clarified the situation by demonstrating a dependence of the saturation level on both η and ν in terms of the magnetic Prandtl number, $P_m = \nu/\eta$. In particular, the level of angular momentum transport increases with increasing P_m for simulations initiated with a uniform as well as vanishing mean magnetic field in the vertical direction (Fromang et al. 2007; Lesur & Longaretti 2007).

Determining the stress levels in MRI turbulence is only one aspect of the problem; another is exploring how that turbulence is dissipated into heat. This question has direct relevance to phenomenological disk models as well as observations. The α model assumes that the accretion energy is deposited as heat locally and rapidly, and Balbus & Papaloizou (1999) showed that this property should hold for the energetics of MHD turbulence as well. In the simulations, we can determine the rate at which turbulent energy is thermalized and the path that energy takes as it moves from the free energy of the shear flow to turbulence and then to heat. Such issues were briefly touched on by Brandenburg et al. (1995) who found that the turbulent magnetic energy was ~ 6 times greater than the perturbed kinetic energy, but dissipational heating resulted from roughly equal contributions of magnetic and kinetic energy dissipation. This result led them to suggest that there was a net transfer of magnetic energy to turbulent kinetic energy. Sano & Inutsuka (2001) studied energy flow in the context of MRI channel modes, which are strong radial streaming motions that result from the linear growth of the vertical field MRI (Hawley & Balbus 1992; Balbus & Hawley 1998). Their work included Ohmic resistivity (but not viscosity) and showed that resistive heating dominated the thermalization of energy stored in these channel modes. Dissipational heating also plays an important role in radiative effects and determining disk structure, both of which may be observable properties of disks (e.g., Beckwith et al. 2008).

In any study that depends on simulations, there remain factors which cannot be overlooked: the effects due to numerics and finite resolution. The majority of the results to-date were obtained with numerical codes based on the finite-difference ZEUS algorithm (Stone & Norman 1992a,b), carried out at relatively low resolution. ZEUS is effectively first-order in asymptotic convergence, and in its most widely used form, evolves the internal rather than the total energy equation. There have been improvements in both the available computational power, which makes higher resolutions and longer evolution times possible, and in the algorithms for compressible MHD. In this work, we will reexamine the properties of MHD turbulence in the shearing box using a higher-order, Godunov scheme.

The new code, Athena, (see Stone et al. 2008) represents an improvement over ZEUS in several ways including true second-order convergence, increased effective resolution (see Stone & Gardiner 2005), accurate shock capturing, and conservation of total energy. The energy-conserving properties of Athena allow us to study energy flow and dissipation within the shearing box in greater detail than allowed for by the ZEUS algorithm. The version of Athena we use in this paper does not include explicit resistivity or viscosity and instead relies on numerical dissipation to thermalize the turbulent energy. Nevertheless, this work will serve as a starting point for planned studies of nonideal effects, including the influence of P_m on the turbulence (Fromang et al. 2007; Lesur & Longaretti 2007). As an important part of establishing a baseline of simulations, we will characterize the numerical resistivity and

viscosity of Athena for the shearing box problem. To do so, we will follow the recent work of Fromang & Papaloizou (2007) who studied the numerical effects of ZEUS on the saturated state of MRI shearing box simulations that begin with zero net field. They found that the amplitude of the turbulence decreases with increasing resolution and developed several useful diagnostics with which to quantify the effective numerical resistivity and viscosity in the problem.

The structure of the paper is as follows. In § 2, we describe the algorithm employed and our simulations. In § 3, we reexamine some of the results from previous MRI studies and provide a comparison with these studies. In § 4, we present the first of two diagnostics used to study turbulent energy flow and dissipation. The second of these diagnostics is applied in § 5. Finally, we discuss our results and summarize our conclusions in § 6.

2. Numerical Simulations

The code used for all of our simulations is Athena, a second-order accurate Godunov scheme for solving the equations of ideal MHD in conservative form. The equations are solved using the dimensionally unsplit corner transport upwind (CTU) method of Colella (1990) coupled with the third-order in space piecewise parabolic method (PPM) of Colella & Woodward (1984) and a constrained transport (CT) algorithm for preserving the $\nabla \cdot \boldsymbol{B} = 0$ constraint. Details of the algorithm are described in Gardiner & Stone (2005a), Gardiner & Stone (2008), and Stone et al. (2008). The Athena code has been extensively tested against various hydrodynamic and MHD tests (Stone et al. 2008).

We employ the shearing box formalism, in which our computational domain is corotating with the fluid flow at some radius in the disk. The domain size is small compared to this radius, allowing us to expand the equations of motion in Cartesian form, as described in detail by Hawley et al. (1995).

In the ideal MHD approximation, the evolution of the fluid in the shearing box is described by:

$$\frac{\partial \rho}{\partial t} + \nabla \cdot (\rho \boldsymbol{v}) = 0, \tag{1}$$

$$\frac{\partial \rho \boldsymbol{v}}{\partial t} + \nabla \cdot (\rho \boldsymbol{v}\boldsymbol{v} - \boldsymbol{B}\boldsymbol{B}) + \nabla (P + \frac{1}{2} B^2) = 2q\rho\Omega^2 \boldsymbol{x} - 2\boldsymbol{\Omega} \times \rho \boldsymbol{v}, \tag{2}$$

$$\frac{\partial \boldsymbol{B}}{\partial t} + \nabla \cdot (\boldsymbol{v}\boldsymbol{B} - \boldsymbol{B}\boldsymbol{v}) = 0, \tag{3}$$

$$\frac{\partial E}{\partial t} + \nabla \cdot [(E + P + \frac{1}{2}B^2)\boldsymbol{v} - \boldsymbol{B}(\boldsymbol{B} \cdot \boldsymbol{v})] = 2q\Omega^2 \rho \boldsymbol{v} \cdot \boldsymbol{x}, \tag{4}$$

where ρ is the mass density, $\rho\boldsymbol{v}$ is the momentum density, $\boldsymbol{B}$ is the magnetic field, P is the gas pressure, E is the total energy density, and q is the shear parameter, defined as $q = -d\ln\Omega/d\ln R$. Ω is the angular velocity of the center of the shearing box. Note that our system of units has the magnetic permeability $\mu = 1$. We use $q = 3/2$, appropriate for a Keplerian disk. The first source term on the right-hand side of equation (2) and the term on the right-hand side of equation (4) correspond to tidal forces (gravity and centrifugal) in the corotating frame. The second source term in equation (2) is the Coriolis force. The total energy density is the sum of the thermal, kinetic, and magnetic energy densities

$$E = \epsilon + \frac{1}{2}\rho v^2 + \frac{1}{2}B^2 \tag{5}$$

where ϵ is thermal energy density. The equation of state is that of an ideal gas, $\epsilon = P/(\gamma - 1)$, where the adiabatic index is $\gamma = 5/3$ in all simulations. The terms on the right hand sides of equations (2) and (4) are added to the MHD equations in a directionally unsplit manner, consistent with the CTU algorithm. Note that we have neglected vertical stratification.

An important component of shearing box simulations is the shearing periodic boundary conditions at the x boundaries, which are implemented as described in Hawley et al. (1995) with a few modifications for Athena. First, as in Hawley et al. (1995), the y momentum is adjusted to account for the shear across the x boundaries as fluid moves out one boundary and enters at the other. Since Athena evolves the total energy, however, this energy must also be adjusted to account for the difference in y momentum across the boundaries. Second, following the description in Hawley et al. (1995), quantities are linearly reconstructed in the ghost zones from appropriate zones in the physical domain that have been shifted along y to account for the shear across the boundary. However, we have found that the precise conservation of a quantity depends on how this reconstruction is performed; the fluxes of a particular conserved quantity must be reconstructed to conserve the quantity to roundoff level. For example, consider the conservation of magnetic flux through the computational domain. For the magnetic flux through the box to be conserved to machine precision, the line integral of the electromotive force (EMF), $\mathcal{E} = -\boldsymbol{v} \times \boldsymbol{B}$, along the boundaries must remain zero. The y and z boundary conditions are periodic, and therefore, the line integrated EMFs along these boundaries cancel. This is not the case with the shearing periodic boundaries, however. Consider the net B_z flux through the grid, which will be conserved if $\mathcal{E}_y = v_z B_x - v_x B_z$ is zero when integrated along both x boundaries. Computing the EMF using ghost zone variables v_z, B_x, v_x, and B_z after reconstruction introduces a truncation error, and the B_z flux is not conserved. This is avoided if we instead perform

the shearing-periodic reconstruction step on $\mathcal{E}_y$ itself. A similar argument applies to mass conservation; one needs to reconstruct the density flux in the shearing boundaries instead of the density itself.[1]

In the code, we only perform this EMF/flux reconstruction for $\mathcal{E}_y$. We have found that conservation of the B_z flux is essential, owing to the strong effect on the turbulence due to a net vertical field. The perfect conservation of B_y is not as important, and as ensuring its precise conservation involves a more complex procedure, we allow the B_y flux to be conserved only to the truncation level. Similarly, the precise conservation of mass has minimal impact on the behavior of the turbulence, and we allow the mass to be conserved to truncation level. We would like to note, however, that because of this, mass is lost during the MRI evolution in our simulations. To quantify the level of mass loss, the total percentage of mass lost over 100 orbits of evolution is $\sim 2\%$ for our highest resolution simulations (see below for a description of our simulations) and $\sim 10\%$ for our lowest resolution simulations; we observe convergence of mass conservation with resolution.

Although Athena conserves total energy, the shearing boundaries do work on the fluid and represent a significant energy source. As was shown in Hawley et al. (1995), one can integrate the total energy plus gravitational potential energy, $E+\rho\Phi$, where $\Phi = q\Omega^2(\frac{L_x^2}{12}-x^2)$, over the domain to obtain

$$\frac{\partial\langle E+\rho\Phi\rangle}{\partial t} = \frac{q\Omega}{L_y L_z}\int_X (\rho v_x \delta v_y - B_x B_y) dy dz, \tag{6}$$

where L_x, L_y, and L_z are the domain sizes in the x, y, and z directions respectively (see below),

$$\delta v_y \equiv v_y + q\Omega x, \tag{7}$$

and the integral is calculated over one of the x boundaries. In our simulations, equation (6) is satisfied to truncation level with the error coming from the tidal potential source term in equation (4). It is possible to rewrite this source term to guarantee that equation (6) is satisfied to roundoff level (see Gardiner & Stone 2005b), but we have found that this makes very little difference to how the total energy evolves.

Gardiner & Stone (2005b) point out that the source terms in the momentum equa-

[1]In principle, the same argument applies to momentum and energy conservation, but these equations are not conserved to machine precision due to the existence of source terms.

tion cannot be written in a purely conservative form and that the x and y momenta are tightly coupled through these terms. In the hydrodynamic limit the source terms account for epicyclic oscillations, and if the epicyclic kinetic energy (see their equation 8) is not conserved to machine precision, coupling between long wavelength modes and epicyclic oscillation modes can result from truncation error. Over time this coupling can artificially increase the kinetic energy. To ensure the conservation of epicyclic energy, Gardiner & Stone (2005b) evolved the angular momentum fluctuations directly rather than the y momentum, casting the equations into a form consistent with uniform epicyclic motion. They then employed a Crank-Nicholson scheme to evolve the source terms that govern the evolution of the momentum fluctuations. In MHD, however, oscillatory epicyclic motion is replaced by unstable, growing MRI modes. Epicyclic kinetic energy is not conserved and these special techniques are not required. Therefore, we use the standard Athena algorithm (e.g., Stone et al. 2008) to evolve the momentum equations.

As was done in the original shearing box simulations (Hawley et al. 1995) our standard shearing box has a radial size $L_x = 1$, an azimuthal size $L_y = 2\pi$, and a vertical size $L_z = 1$. We initialize a velocity flow with $\boldsymbol{v} = -q\Omega x\hat{\boldsymbol{y}}$, with $q = 3/2$, $\Omega = 0.001$, and $-L_x/2 \leq x \leq L_x/2$. In an isothermal disk, the sound speed is $c_{\rm s} \sim \Omega H$ where H is the scale height. With $L_z = H$, we have $c_{\rm s} = L_z\Omega$, and we define the initial pressure as $P = \rho\Omega^2 L_z^2$. With $\rho = 1$, we have $P = 10^{-6}$. In this paper, we consider two initial magnetic field geometries that are commonly used in shearing box studies. Models labeled NZ (for Net Z-field) have an initial uniform vertical magnetic field, B_z, and models labeled SZ (for Sine Z-field) begin with a sinusoidal distribution of B_z and have zero net flux through the box. Specifically, we initialize the NZ runs with $\boldsymbol{B} = \sqrt{2P/\beta}\,\hat{\boldsymbol{z}}$, and the SZ runs with $\boldsymbol{B} = \sqrt{2P/\beta}\sin[(2\pi/L_x)x]\hat{\boldsymbol{z}}$. In both cases, we set $\beta = 1600$. This determines the ratio of the vertical box size to the fastest growing linear MRI wavelength as $L_z/\lambda_c \sim 4$, where $\lambda_c = 2\pi\sqrt{16/15}|v_{\rm A}|/\Omega$, and $v_{\rm A}$ is the Alfvén speed. To seed the MRI, we introduce random adiabatic perturbations to P and ρ with amplitude $\delta P/P = 0.01$.

For both of these initial field configurations, we have run a full range of grid resolutions, from $N_x = 16$, $N_y = 32$, $N_z = 16$ to the highest resolution used in this study, $N_x = 128$, $N_y = 256$, $N_z = 128$, proceeding by factors of two. All of the simulations were run for a total of 100 orbits.

In addition to the standard shearing box simulations, we have run some additional experiments designed to further investigate magnetic and kinetic energy dissipation. First, we perform a set of simulations in which we remove the velocity shear and the tidal and Coriolis force terms, thus removing the energy source that maintains the turbulence. The purpose of these simulations is to investigate energy flow and dissipation in the absence

of the shear, which is the driving force for the turbulence. We perform these simulations by restarting each of the standard shearing box runs at a time when the shearing periodic boundaries are strictly periodic. These "periodic points" are given by $t_n = n\,L_y/q\,\Omega\,L_x$, with $n = 0, 1, 2, ...$, (see Hawley et al. 1995). We choose the restart time to be 40 orbits. We then evolve the system to follow the decay of the kinetic and magnetic energies.

Finally, we run a set of low resolution simulations with varying aspect ratio to examine the effect of secondary parasitic modes on the channel solution (see § 3.2). These simulations have the same initial conditions as the net flux simulation with $N_x = 32$, $N_y = 64$, and $N_z = 32$ but with varying domain size in the x and y dimensions. The grid cell size (e.g., L_x/N_x in the x direction) in each dimension is kept constant. All simulations are summarized in Table 1.

Table 1. MRI Simulations with Athena

Label	Initial Field Geometry	Resolution ($N_x \times N_y \times N_z$)	Domain ($L_x \times L_y \times L_z$)	Description
NZ16	net flux	$16 \times 32 \times 16$	$1 \times 2\pi \times 1$	–
NZ32	net flux	$32 \times 64 \times 32$	$1 \times 2\pi \times 1$	–
NZ64	net flux	$64 \times 128 \times 64$	$1 \times 2\pi \times 1$	–
NZ128	net flux	$128 \times 256 \times 128$	$1 \times 2\pi \times 1$	fiducial run - net flux
NZD128	net flux	$128 \times 256 \times 128$	$1 \times 2\pi \times 1$	decaying turbulence
SZ16	zero net flux	$16 \times 32 \times 16$	$1 \times 2\pi \times 1$	–
SZ32	zero net flux	$32 \times 64 \times 32$	$1 \times 2\pi \times 1$	–
SZ64	zero net flux	$64 \times 128 \times 64$	$1 \times 2\pi \times 1$	–
SZ128	zero net flux	$128 \times 256 \times 128$	$1 \times 2\pi \times 1$	fiducial run - zero net flux
SZD128	zero net flux	$128 \times 256 \times 128$	$1 \times 2\pi \times 1$	decaying turbulence
NZAR1	net flux	$16 \times 64 \times 32$	$\frac{1}{2} \times 2\pi \times 1$	varied aspect ratio
NZAR2	net flux	$64 \times 64 \times 32$	$2 \times 2\pi \times 1$	varied aspect ratio
NZAR3	net flux	$32 \times 32 \times 32$	$1 \times \pi \times 1$	varied aspect ratio
NZAR4	net flux	$16 \times 32 \times 32$	$\frac{1}{2} \times \pi \times 1$	varied aspect ratio
NZAR5	net flux	$64 \times 32 \times 32$	$2 \times \pi \times 1$	varied aspect ratio
NZAR6	net flux	$128 \times 32 \times 32$	$4 \times \pi \times 1$	varied aspect ratio

3. General Properties of MRI Turbulence

This work represents the first detailed study of the MRI with Athena, which has an algorithm significantly different from that used in ZEUS. To begin, we will reexamine many of the shearing box models and the results already documented in the literature. Any significant differences between Athena results and those previously published could indicate where numerical effects (algorithm, resolution) have an influence. Since Athena is an energy-conserving, shock-capturing algorithm it has at least the potential to produce somewhat different results. Conversely, agreement between Athena and other codes would support the robustness of the shearing box results to date.

In this section, we describe some of the general properties of MRI turbulence as simulated with Athena and compare our results with those in the literature. These properties will also serve as a starting point for further analysis presented in the following sections. In what follows, the highest resolution runs NZ128 and SZ128 will serve as our fiducial simulations for each initial field geometry. We study resolution effects for each field geometry using the lower resolution simulations.

3.1. Characteristics of Saturation

Figures 1 and 2 show the development of the MRI and the subsequent evolution of the resulting MHD turbulence for the fiducial NZ128 and SZ128 runs respectively. The MRI saturates before orbit 5 and the MHD turbulent state lasts for the remainder of the 100 orbit simulation. Along with these figures, we list several time- and volume-averaged quantities from the fiducial runs in Table 2. The time average is done from orbits 20 to 100, and the errors are given by one standard deviation over this period. Volume-averaged values are indicated by the single-angled bracket notation (e.g., $\langle B^2 \rangle$), and time- and volume-averaged values are denoted by double-angled brackets (e.g., $\langle\langle B^2 \rangle\rangle$). In both fiducial runs, the toroidal field magnetic energy dominates with $\langle B_y^2/2 \rangle > \langle B_x^2/2 \rangle > \langle B_z^2/2 \rangle$. Examining the components of the kinetic energy and perturbed kinetic energy, which is $(\rho/2)(v_x^2 + \delta v_y^2 + v_z^2)$ with δv_y given by equation (7), we find they are closer to each other in value than are the components of the magnetic energy. The relative ordering is similar except that the x kinetic energy is larger than the perturbed y kinetic energy, $\rho \delta v_y^2/2$, in SZ128. Another feature of note is the greater saturation level and fluctuation amplitude of the NZ128 run compared to that of SZ128. As in past studies, the Maxwell stress dominates over the Reynolds; the ratio of the Maxwell to Reynolds stress oscillates between 1 and 10. Similarly, past studies have shown a tight correlation between Maxwell (and total) stress and the magnetic energy density (see, e.g., Blackman et al. 2008). Here the ratio of the Maxwell stress to the magnetic energy

density is roughly 1/2. These values and the overall observations are generally consistent with the results of Hawley et al. (1995), Hawley et al. (1996), and Sano et al. (2004).

One major difference from past ZEUS simulations is the evolution of the total ($E + \rho\Phi$) and thermal (ϵ) energy densities, shown in the lower right plot of Figs. 1 and 2 for the NZ128 and SZ128 runs respectively. Since we evolve an adiabatic equation of state and there is no cooling term in the energy equation, the total energy increases with time at a rate given by equation (6). The total energy increases because the free energy of the shearing fluid is being thermalized by the turbulence, but the shearing box boundary conditions continuously reinforce that shear. The stresses at the radial boundaries therefore constitute a source term. Equation (6) also explains why the total energy reaches a higher value at the end of the simulation in NZ128 compared to SZ128. Since the volume-averaged stress (which is roughly equal to the stress at the radial boundaries) is higher in NZ128, the energy injection rate will be larger. These plots also show that the thermal energy follows the total energy very closely. That is, the injected energy ends up as thermal energy a short time later (Gardiner & Stone 2005b). We will further study the thermalization of injected energy in §4 and §5.

Does the significant increase in thermal energy affect the turbulence in any way? This question was examined by Sano et al. (2004) in an extensive series of simulations. They found evidence of a very weak dependence of the time-averaged Maxwell stress on the gas pressure. Such an increase is not apparent from a first look at Figs. 1 and 2, but short timescale fluctuations are a dominant feature of these volume-averaged quantities. We examined the long term behavior of the Maxwell stress using time-averaging procedures to smooth away the fluctuations (which do not appear to change over long timescales). We found marginal evidence for a weak dependence of the Maxwell stress on the gas pressure in some, but not all, of the data. While it is possible that longer evolution times and a wider exploration of parameter space could be useful to address this question further, it is clear the stress has barely changed despite an increase in thermal pressure by a factor of order 100 in run NZ128. Thus if there is any dependence of the stress on the pressure, it is very weak and does not significantly affect the characteristics of local MRI turbulence.

We study the effect of resolution through a series of lower resolution simulations (see Table 1). Figure 3 shows the time- and volume-averaged magnetic and perturbed kinetic energies as a function of grid resolution for both the net flux and zero net flux initial conditions. The time average is calculated from orbits 20 to 100; the error bars indicate one standard deviation. For the net flux simulation, there appears to be a slight trend of increasing energy with resolution, as observed in Hawley et al. (1995). Resolution has a more obvious effect on the zero net flux initial condition. The turbulent energies *decrease* with increasing resolution. This resolution effect was previously reported for zero net field initial

conditions in other simulations (Fromang & Papaloizou 2007; Pessah et al. 2007) using different numerical algorithms. With Athena, the time- and volume-averaged total magnetic energy density decreases by roughly a factor of two for each factor of two resolution increase. The amplitude of the fluctuations in the total magnetic energy density decreases by roughly a factor of two to four for each resolution increment. At all resolutions, the y magnetic energy density continues to be the largest, followed by the x energy, and then the z energy. As was the case for NZ128, $\rho\delta v_y^2/2$ dominates for all net flux simulations, followed by $\rho v_x^2/2$, and then $\rho v_z^2/2$. In the zero net flux simulations, the x kinetic energy density is greater than the perturbed y kinetic energy density. These components of the perturbed kinetic energy density are close in value, and it is often the case that the x and y components are within one standard deviation of each other. The ratio of time- and volume-averaged Maxwell stress to time- and volume-averaged magnetic energy density is constant with resolution. The ratio of time- and volume-averaged Maxwell stress to time- and volume-averaged Reynolds stress has a slight increase with resolution in the net flux simulations and a slight decrease with resolution in the zero net flux simulations. However, we point out that the observed trends in the ratio of stresses are subject to considerable uncertainty given the large error bars calculated for the various quantities.

3.2. Channel Solution

One of the interesting aspects of the vertical field MRI in a shearing box is that the fastest growing mode leads to axisymmetric radial streaming motions, dubbed "channel solutions" (Hawley & Balbus 1992). Goodman & Xu (1994) pointed out that for the vertical field in an unstratified box, the linear MRI eigenmode is also a nonlinear solution in the incompressible limit. They further show that the nonlinear channel solution is itself unstable to "parasitic modes." These modes require radial and azimuthal wavelengths larger than the vertical wavelength of the channel solution and will disrupt the channel flow if the box is large enough (Balbus & Hawley 1998).

In the present simulations, the initial vertical field is sufficiently weak that the fastest growing vertical wavelength is less than the radial and azimuthal dimensions of the box, and any initial tendency toward the channel solution at the end of the linear growth phase is quickly disrupted. However, we find that the large fluctuations in the magnetic energy density for NZ128 are a result of recurring channel solutions.[2] Figure 4 shows the azimuthally-

[2] The recurrence of the channel solution presumably results from the fact that the net vertical magnetic field can never be destroyed or removed from the domain, given the periodic boundary conditions and the

averaged velocities at several times during the amplification and subsequent decay of one such fluctuation. The flow organizes itself into a two-channel solution, which becomes more well-defined as the magnetic energy increases. The channel solution is eventually destroyed via secondary, parasitic instabilities (see Goodman & Xu 1994), which coincides with a decrease in magnetic energy. The same channel solution appears during other instances of large magnetic energy fluctuation in NZ128 and does not appear in SZ128. Furthermore, the recurring channel flows appear in the lower resolution net magnetic flux simulations. As observed previously, the channel solution and large magnetic energy fluctuations are a property of simulations with a uniform B_z field (Sano & Inutsuka 2001).

Since the channel solution is subject to parasitic modes that depend on the available wavelengths that can fit in the box, we expect that this behavior is influenced by the domain aspect ratio employed. To verify this, we have run several low resolution simulations (labelled NZAR1 − NZAR6, see § 2) using different aspect ratios. We found that for large enough L_x, the intermittent channel modes no longer occur; this behavior was also observed by Bodo et al. (2008). The prominence of intermittent channel flows is a consequence of the restrictions introduced by the domain size. However, we use this property in § 4, where the large fluctuations in turbulent energy created by the channel solutions provide a clear marker of energy injection by the boundaries. We can then track the subsequent thermalization of that energy.

3.3. Energy Power Spectra

The nature of MRI-driven MHD turbulence can be characterized in part by the power spectrum of kinetic and magnetic energies. To obtain such power spectra, we do a full 3D Fourier transform on the simulation data employing the procedures outlined in Hawley et al. (1995) to account for the shearing-periodic boundaries. Briefly, the shearing periodic boundary conditions in the x direction allow the domain to be strictly periodic in the x direction only at certain times, called periodic points t_n (described in §2). To perform a standard fast Fourier transform (FFT) at some time t that is not equal to t_n, we transform the data into a frame where the x boundaries are strictly periodic. We then calculate the FFT in this frame and remap to the original frame.

The turbulent magnetic, kinetic, and perturbed kinetic energy densities in Fourier space are defined as

---

strict conservation of z magnetic flux.

$$\frac{1}{2}|\widetilde{\boldsymbol{B}}(\boldsymbol{k})|^2 \equiv \frac{1}{2}\left[|\widetilde{B_x}(\boldsymbol{k})|^2 + |\widetilde{B_y}(\boldsymbol{k})|^2 + |\widetilde{B_z}(\boldsymbol{k})|^2\right], \tag{8}$$

$$\frac{1}{2}|\widetilde{\sqrt{\rho}\boldsymbol{v}}(\boldsymbol{k})|^2 \equiv \frac{1}{2}\left[|\widetilde{\sqrt{\rho}v_x}(\boldsymbol{k})|^2 + |\widetilde{\sqrt{\rho}v_y}(\boldsymbol{k})|^2 + |\widetilde{\sqrt{\rho}v_z}(\boldsymbol{k})|^2\right], \tag{9}$$

$$\frac{1}{2}|\widetilde{\sqrt{\rho}\boldsymbol{\delta v}}(\boldsymbol{k})|^2 \equiv \frac{1}{2}\left[|\widetilde{\sqrt{\rho}v_x}(\boldsymbol{k})|^2 + |\widetilde{\sqrt{\rho}\delta v_y}(\boldsymbol{k})|^2 + |\widetilde{\sqrt{\rho}v_z}(\boldsymbol{k})|^2\right], \tag{10}$$

where $\widetilde{f}$ means the Fourier transform of f defined by

$$\widetilde{f(\boldsymbol{k})} = \int\int\int f(\boldsymbol{x})\mathrm{e}^{-i\boldsymbol{k}\cdot\boldsymbol{x}}\mathrm{d}^3\boldsymbol{x}. \tag{11}$$

Note that for the kinetic energies, we include the density along with the velocity when calculating the Fourier transform, resulting in the appearance of $\sqrt{\rho}$ in the above equations. To obtain these quantities as a function of length scale and to improve statistics, we average our data over shells of constant $k = |\boldsymbol{k}|$. For further improvement of statistics, we average each of these terms over 161 frames (i.e., from orbit 20 to 100 in increments of 0.5 orbits).

Figure 5 shows the power spectra of these energy densities for the net flux and zero net flux runs. The figure shows resolution effects as different lines in each plot. In all cases, the largest scales account for most of the energy. The general shape of the energy power spectra agrees with previous studies (e.g., Hawley et al. 1995; Fromang & Papaloizou 2007). For the net flux simulations, the magnetic energy dominates over the kinetic and perturbed kinetic energies at all scales, independent of resolution. As the resolution is increased, the power spectra extend to higher k, but the general shape remains constant. At some values for k, the uncertainty in energy (not plotted), represented by one temporal standard deviation around the mean, is large enough to overlap with other energy components, making it difficult to conclusively say which energy dominates at these particular scales.

We calculated a power law index in Fourier space for each energy density and at each resolution. This slope was determined by a linear fit to the energy densities in log space from $kL/(2\pi) = 1$ to the maximum scale for the given resolution. There is some uncertainty in this measurement because the power spectra are not strictly linear in log space (see Fig. 5). In NZ128, the energy density is proportional to $[kL/(2\pi)]^n$ with $n \approx -4$ for every energy density. This index is approximately constant with resolution, but there is evidence that n becomes more negative at higher resolutions. In determining an error in the value of n, we found that this error is often dominant. Thus, such a resolution dependence is somewhat tentative.

There is a noticeable resolution dependence in the zero net flux simulations. First, as resolution is increased, the magnetic energy density decreases at all scales. This effect was discussed in § 3.1; the power spectra are consistent with the power spectrum analysis of Fromang & Papaloizou (2007). The same resolution dependence is observed for the perturbed kinetic energy density. The magnetic energy density at small k decreases faster with resolution than does the perturbed kinetic energy density. The total kinetic energy density (i.e., including shear) remains constant with resolution, which simply results from the fact that the shear velocity, which dominates the kinetic energy, is constant with resolution. The uncertainty in each energy component appears to be smaller than in the net flux simulations. However, there are still some values of k at which the calculated errors overlap.

We calculated a power law index in Fourier space for each energy density and resolution for the zero net flux simulations. The procedure we used was the same as for the net flux simulations. For the kinetic and perturbed kinetic energy densities, we found that n lies between -3.5 and -4, whereas for the magnetic energy density, n lies between -3 and -3.5. There does not appear to be any resolution dependence in n for the magnetic energy density, but there is a tentative decrease in n (similar to the net flux case) with increasing resolution for the kinetic and perturbed kinetic energy densities.

Table 2. Saturation Characteristics

Quantity	NZ128	SZ128
$\langle\langle -B_x B_y \rangle\rangle / P_o$	0.216 ± 0.116	$(6.55 \pm 1.15) \times 10^{-3}$
$\langle\langle \rho v_x \delta v_y \rangle\rangle / P_o$	0.028 ± 0.019	$(1.91 \pm 0.76) \times 10^{-3}$
$\langle\langle B^2/2 \rangle\rangle / P_o$	0.488 ± 0.262	0.014 ± 0.003
$\langle\langle B_x^2/2 \rangle\rangle / P_o$	0.071 ± 0.027	$(2.01 \pm 0.38) \times 10^{-3}$
$\langle\langle B_y^2/2 \rangle\rangle / P_o$	0.388 ± 0.231	0.011 ± 0.002
$\langle\langle B_z^2/2 \rangle\rangle / P_o$	0.029 ± 0.011	$(7.98 \pm 1.57) \times 10^{-4}$
$\langle\langle \rho \delta v^2/2 \rangle\rangle / P_o$	0.145 ± 0.060	$(7.69 \pm 1.81) \times 10^{-3}$
$\langle\langle \rho v_x^2/2 \rangle\rangle / P_o$	0.046 ± 0.024	$(3.73 \pm 1.27) \times 10^{-3}$
$\langle\langle \rho \delta v_y^2/2 \rangle\rangle / P_o$	0.078 ± 0.035	$(2.68 \pm 0.60) \times 10^{-3}$
$\langle\langle \rho v_z^2/2 \rangle\rangle / P_o$	0.021 ± 0.011	$(1.28 \pm 0.21) \times 10^{-3}$
$\langle\langle -B_x B_y \rangle\rangle / \langle\langle \rho v_x \delta v_y \rangle\rangle$	7.60 ± 6.47	3.43 ± 1.49
$\langle\langle -B_x B_y \rangle\rangle / \langle\langle B^2/2 \rangle\rangle$	0.443 ± 0.336	0.462 ± 0.116

4. Energy Fluctuations

Athena evolves the equation for total energy, the volume-average of which will change only due to the Maxwell and Reynold stresses at the radial boundaries (equation (6)). As was discussed in §3, the individual volume-averaged magnetic and kinetic energies are highly variable throughout the evolution as energy is continuously transferred between magnetic, kinetic and thermal components. We can study these energy flow processes by tracking the energy injected at the boundaries as it is subsequently thermalized in the turbulence. For this purpose, the existence of the recurring channel solution in the net magnetic field simulation is very useful; the sudden increase in stress provides a clear injection of energy that can be traced using several diagnostics. Having developed these diagnostics we can then apply them to the zero net magnetic flux simulations. Finally, to gain additional insight into dissipation in the turbulence, we conduct an experiment in which the shear flow and gravity terms have been removed.

4.1. Sustained Turbulence

The total energy density, including the gravitational potential energy density, is defined as

$$E_{\rm tot} = E + \rho\Phi = \epsilon + \frac{1}{2}\rho v^2 + \frac{1}{2}B^2 + \rho\Phi \tag{12}$$

where Φ is given in §2. Averaging equation (12) over the entire domain, taking the time derivative, and rearranging the terms, we obtain,

$$\dot{T} = E_{\rm in} - \dot{K} - \dot{M} - \dot{G}. \tag{13}$$

where $E_{\rm in} \equiv \partial\langle E_{\rm tot}\rangle/\partial t$ is the energy injection rate due to stress at the boundaries (see equation (6)), $\dot{T} \equiv \partial\langle\epsilon\rangle/\partial t$ is the rate of change of thermal energy density, $\dot{K} \equiv \partial\langle\frac{1}{2}\rho v^2\rangle/\partial t$ is the rate of change of the kinetic energy density, $\dot{M} \equiv \partial\langle\frac{1}{2}B^2\rangle/\partial t$ is the rate of change of the magnetic energy density, and $\dot{G} \equiv \partial\langle\rho\Phi\rangle/\partial t$ is the time derivative of the tidal potential energy density. The brackets indicate a volume-average over the simulation domain. $\dot{G}$ is the change in a fluid element's gravitational energy as it moves within the domain. We expect the contribution of the tidal potential term to be insignificant, an expectation borne out by direct computation. We will ignore this term in most of the subsequent discussion. The stress terms at the radial boundaries are generally positive, which means energy is being

injected into the box via the work done by this stress ($E_{\rm in} > 0$). The remaining terms in equation (13) can be either positive or negative.

The lower right plot in Figure 1 shows that the thermal energy density closely follows the total energy density, but with a short time delay. This can be better seen in Figure 6, which shows the individual terms from equation (13) for a 20 orbit period in the NZ128 simulation. There is a clear time delay of less than one orbit between significant changes in the energy injection rate and the thermal energy derivative, suggesting a comparable delay before the injected energy is thermalized, a property noted in Sano & Inutsuka (2001) as well as in Gardiner & Stone (2005b). These features in the energy derivatives result from the creation and destruction of channel flows. During this time interval, the magnetic and kinetic energies are also changing. By examining the maxima in the thermal energy derivative and the corresponding features in the kinetic and magnetic energy derivatives, it appears that the magnetic energy dissipation dominates the thermalization process.

It is useful to define a temporal correlation function for the various energy components by writing

$$C_{AB} \equiv \begin{cases} \dfrac{\dfrac{1}{N-|L|}\displaystyle\sum_{i=0}^{N-|L|-1} A_{i+|L|}B_i}{\dfrac{1}{N}\displaystyle\sum_{i=0}^{N-1} A_i} & \text{if } L < 0 \\ \dfrac{\dfrac{1}{N-|L|}\displaystyle\sum_{i=0}^{N-L-1} A_i B_{i+L}}{\dfrac{1}{N}\displaystyle\sum_{i=0}^{N-1} A_i} & \text{if } L \geq 0 \end{cases} \tag{14}$$

where A and B are two time-series datasets N elements in length. The quantity L is the number of elements over which to shift A and B with respect to each other to calculate the correlation coefficient. We apply equation (14) to the energy rates by setting $A = \dot{T}$, and $B = \dot{K}$, $\dot{M}$, or $E_{\rm in}$. This allows us to correlate the energy injection rate and the change in kinetic and magnetic energies against the change in thermal energy over certain timescales. Since $\dot{T} > 0$, if the correlation between $\dot{T}$ and $\dot{K}$ (or $\dot{M}$) is negative, then kinetic energy (or magnetic energy) must be decreasing, and a strong negative correlation would suggest that kinetic energy (or magnetic energy) is being thermalized.

Figure 7 is the correlation function for $B = E_{\rm in}, \dot{K}$, and $\dot{M}$ calculated over orbits 20 to 100. The x-axis is the correlation timescale in units of orbits. We only look at correlation

times of $\lesssim 1$ orbit as the degree to which the thermal energy evolution follows that of the total energy (see Figures 1 and 2) indicate that thermalization happens over that timescale. To examine the correlation function on longer timescales would be misleading since peaks in the function would suggest a correlation between two events that are not causally related (e.g., the injection of energy for one channel event being correlated with the thermalization of energy for another channel event). The left plot of the figure shows that $E_{\rm in}$ is strongly correlated with $\dot{T}$ on a timescale of $\Delta t \sim$ -0.2 orbits. This correlation is exactly what we observed in Fig. 6. The energy injected by the stress at the boundaries ends up as heat less than one orbit later. The negative sign on this value of Δt simply means that the injection happens before the thermalization. In the right plot, both $\dot{K}$ and $\dot{M}$ are negatively correlated with $\dot{T}$ suggesting that magnetic and kinetic energy are being thermalized. The stronger magnetic correlation further suggests that magnetic dissipation contributes more to thermalization than kinetic dissipation. The positive correlation between $\dot{K}$ and $\dot{M}$ against $\dot{T}$ at negative Δt values is a result of the magnetic and kinetic energies increasing along with the energy injection into the box. That is, the stress at the boundaries increases the magnetic and kinetic energies which are dissipated a short time later.

An interesting feature is evident in Fig. 7: the negative peak in the magnetic and kinetic correlation functions occur for Δt slightly greater than zero. Similarly, in Fig. 6 one can see that peaks in the magnetic and kinetic energy derivatives are offset with respect to the energy injection and thermalization peaks. For example, the maximum rate for magnetic energy loss occurs after the maximum rate for thermal energy gain. Of course, these are plots of the time derivative of the energy, so a peak simply indicates where the second derivative is zero. The magnetic energy is both losing energy to dissipation while gaining energy from the shear at the boundaries. When the energy injection rate peaks decline, the thermalization rate is still growing and the magnetic energy rate also peaks and begins to decline. Similarly, the slope of the magnetic energy loss rate will change sign after the thermalization rate has peaked and when the energy injection rate is no longer itself in decline.

As a test, we performed this correlation analysis on the lower resolution net-flux simulations and find that energy injection precedes thermalization by ~ 0.2 orbits, independent of resolution. Furthermore, magnetic dissipation dominates over kinetic dissipation for all net flux simulations.

The analysis so far has only examined the rate of change in the energy terms, not specifically how they change. For example, does a "dip" in $\dot{M}$ correspond to direct thermalization of magnetic energy, or is there a transfer of energy from magnetic to kinetic? To examine the energy flow in more detail, we focus on orbits 50 to 52 in NZ128, for which we ran the NZ128 simulation at high temporal resolution. This high time resolution allows us to resolve short

timescale features, but also generates many large data files. Therefore, we restrict this part of the analysis to the two orbit period mentioned above. Consider the evolution equation for the volume-averaged kinetic energy given by

$$\begin{aligned}\dot{K} &= -\left\langle \nabla \cdot \left[\boldsymbol{v} \left(\frac{1}{2}\rho v^2 + \frac{1}{2}B^2 + P + \rho\Phi \right) - \boldsymbol{B}(\boldsymbol{v}\cdot\boldsymbol{B}) \right] \right\rangle \\ &\quad + \left\langle \left(P + \frac{1}{2}B^2 \right) \nabla \cdot \boldsymbol{v} \right\rangle - \langle \boldsymbol{B} \cdot (\boldsymbol{B} \cdot \nabla \boldsymbol{v}) \rangle - \dot{G} - \dot{Q}_{\rm k}, \end{aligned} \tag{15}$$

where $\dot{Q}_{\rm k}$ is the volume-averaged (numerical) kinetic energy dissipation rate. The evolution equation for the volume-averaged magnetic energy is given by

$$\dot{M} = -\left\langle \nabla \cdot \left(\frac{1}{2}B^2 \boldsymbol{v} \right) \right\rangle - \left\langle \frac{1}{2}B^2 \nabla \cdot \boldsymbol{v} \right\rangle + \langle \boldsymbol{B} \cdot (\boldsymbol{B} \cdot \nabla \boldsymbol{v}) \rangle - \dot{Q}_{\rm m} \tag{16}$$

where $\dot{Q}_{\rm m}$ is the volume-averaged (numerical) magnetic energy dissipation rate. We have calculated each term in these equations over the two orbit period and find that the dominant terms are $-\langle \nabla \cdot (\frac{1}{2}\rho v^2)\boldsymbol{v} \rangle$, $\langle \nabla \cdot [\boldsymbol{B}(\boldsymbol{v}\cdot\boldsymbol{B})] \rangle$, $\langle \boldsymbol{B} \cdot (\boldsymbol{B} \cdot \nabla \boldsymbol{v}) \rangle$, $\dot{Q}_{\rm k}$, and $\dot{Q}_{\rm m}$. $\dot{Q}_{\rm k}$ and $\dot{Q}_{\rm m}$ are what remain after calculating all other terms in the energy equations at a particular instant in time. Calculating the volume-averages of the first two terms yields the radial boundary Reynolds and Maxwell stresses in Equation (6) (Hawley et al. 1995), namely the energy injection rate by the shearing periodic boundaries. The third of the dominant terms is the transfer rate of kinetic to magnetic energy via field line stretching. Figure 8 plots the time-history of this term (pink line) along with $\dot{T}$ (black line), the energy injection rate $E_{\rm in}$ (blue line), and $-\dot{Q}_{\rm k}$ and $-\dot{Q}_{\rm m}$ (green and red lines, respectively). As energy is injected into the grid, a significant fraction of this energy is transferred to the magnetic field via field line stretching, presumably through the shear flow. Thermalization follows 0.2 orbits later and is marked by increases in the absolute value of $\dot{Q}_{\rm k}$ and $\dot{Q}_{\rm m}$, with $|\dot{Q}_{\rm m}| > |\dot{Q}_{\rm k}|$. The ratio of kinetic to magnetic dissipation is approximately constant in time over this period, with $\dot{Q}_{\rm k}/\dot{Q}_{\rm m} \approx 0.6$. This suggests that the details of the thermalization do not vary with intermittent increases in $E_{\rm in}$ that occur when the fluid experiences a channel flow.

As discussed, the recurring channel modes in the net flux simulations create distinguishable points of energy injection that make it straightforward to follow the subsequent thermalization. Such modes do not exist in the zero net flux simulations, which makes the identification of specific correlations slightly more difficult. The situation is further complicated by the overall reduced levels of the turbulence which causes the time derivative of the thermal energy to be dominated by very high frequency oscillations due to propagating

spiral density waves (Gardiner & Stone 2005b). We have determined that these waves are created by compressibility and have very little effect on the dissipational heating within the box. To remove their dominance in the energy derivatives, we rebin the time data using a "neighborhood" averaging procedure in which the rebinned data points are calculated from averages of a specified number of original data points. We then apply equation (14) between $E_{\rm in}$ and $\dot{T}$; the result is shown in Fig. 9. The correlation curve has several narrow peaks, which result from residual effects of the rebinning process. The curve has a broader peak near $\Delta t \sim$ -0.2 orbits, which agrees with the same curves for NZ128 (Fig. 7). The correlation function for SZ128 is not as sharply peaked as that for NZ128, which is most likely a result of the lower amplitude variability in the rebinned SZ128 data. Applying this analysis to the lower resolution zero net flux simulations, we find that the correlation function always has a broad peak at $\Delta t \sim$ -0.2 orbits. Thus, as was the case in the net flux simulations, the energy injection/thermalization timescale is independent of resolution.

Finally, we note that the saturated state of SZ128 is too complex to obtain correlations between $\dot{M}$, $\dot{K}$, and $\dot{T}$, such as was done for NZ128. In the net flux simulations, the recurring channel modes lead to the build up and thermalization of magnetic energy. The creation and thermalization of magnetic energy are events that are well-separated in time, making it easy to study the flow of energy between various components. In the zero net flux simulations, however, the average properties of the turbulence remain more constant in time. We will further investigate the dissipation of magnetic and kinetic energy for the zero net flux geometry in §4.2 and §5.1.

4.2. Decaying Turbulence

As noted by Hawley et al. (1995), the MHD turbulence decays without differential rotation to sustain the MRI. We make use of this to observe how rapidly thermalization occurs when there is no further input of energy. This analysis should provide some additional insight into the thermalization process for each field geometry. We remove the net shear flow and the Coriolis and tidal forces from a state taken from the sustained MRI turbulence in the fiducial models. These runs are labeled "NZD" and "SZD" in Table 1 and are described in more detail in §2. Figure 10 shows the subsequent magnetic and kinetic energy decay for both runs. In the figure, the kinetic and magnetic energies have been normalized to their values at the starting time of $t = 40$ orbits.

In NZD128, the ratio of total magnetic to kinetic energy at $t = 40$ orbits is 3.4. The figure shows that the magnetic energy decays more rapidly than the kinetic energy at early times, losing almost half its initial value within 0.2 orbits. In SZD128, the ratio of total

magnetic to kinetic energy at $t = 40$ orbits is 1.4. The kinetic energy shows high frequency oscillations about an average value that decays in time. These oscillations are due to the same compressive, spiral waves that exist in the sustained turbulence simulations. The magnetic energy is unaffected by these waves. The average decay of kinetic energy, calculated from smoothing away the oscillations, is also shown in the figure. Both the kinetic and magnetic energies decay quickly over time. Again, almost half the magnetic energy is lost within 0.2 orbits. The high frequency oscillations also decay in amplitude over time. As was the case in NZD128, the magnetic dissipation rate is initially faster than that for the kinetic energy. After about one orbit, the decay rates become comparable.

Finally, we checked the contributions from the various terms in equations (15) and (16). In both NZD128 and SZD128, there is some transfer from magnetic to kinetic energy during the decay. However, the transfer rate is small compared to the decay rate of the magnetic energy and is such that the numerical dissipation of magnetic energy dominates over that of kinetic energy.

5. Transfer Functions

In their investigation of convergence of zero net flux shearing box simulations, Fromang & Papaloizou (2007) carried out an analysis based on the evolution of magnetic energy in Fourier space. This analysis shows how magnetic energy is created, transferred from one scale to another, and finally lost due to numerical dissipation. Their study used the ZEUS code and assumed an isothermal equation of state. Here we repeat and expand upon their analysis to understand dissipation as a function of length scale in Athena.

We note several differences between our work and that of Fromang & Papaloizou (2007). First, they focus on magnetic energy evolution and did not provide a comparable calculation for the kinetic energy. Second, recognizing that the y direction is dominated by the largest scales, they restricted their analysis to axisymmetric modes, namely $k_y = 0$. Finally, as they were primarily interested in how poloidal field could be regenerated as part of a dynamo process, a portion of their analysis concentrated on the poloidal components rather than the full magnetic field. We have chosen to extend the Fromang & Papaloizou (2007) analysis more generally to include a kinetic energy density evolution, nonaxisymmetric effects, and the effects of a nonzero toroidal field.

Following Fromang & Papaloizou (2007), we decompose the velocity field of the flow into the mean flow, $\boldsymbol{V}_{\rm sh}$, and the turbulent velocity, $\boldsymbol{v}_{\rm t}$, via

$$\boldsymbol{v} = \boldsymbol{V}_{\rm sh} + \boldsymbol{v}_{\rm t}. \tag{17}$$

The mean flow is defined as

$$\boldsymbol{V}_{\rm sh} = V_{\rm sh}\hat{\boldsymbol{y}} = \frac{\hat{\boldsymbol{y}}}{L_y L_z}\int\int v_y(x,y,z){\rm d}y{\rm d}z. \tag{18}$$

Turning next to the induction equation, we substitute equation (17) for the velocity, take the Fourier transform, and dot the result with the complex conjugate of $\widetilde{\boldsymbol{B}}(\boldsymbol{k})$, which is defined by equation (11) with $f = \boldsymbol{B}$. All Fourier transforms are done via equation (11) using a standard FFT and replacing f with the appropriate quantity. The data is mapped into a frame in which the x boundaries are periodic and then remapped into the original frame after performing the FFT.

The result of this calculation is an equation describing the magnetic energy density evolution in Fourier space,

$$\frac{1}{2}\frac{\partial|\widetilde{\boldsymbol{B}}(\boldsymbol{k})|^2}{\partial t} = A + S + T_{bb} + T_{{\rm div}v} + T_{bv} + D_{\rm mag}, \tag{19}$$

where

$$A = -Re\left[\widetilde{\boldsymbol{B}}^{\boldsymbol{*}}(\boldsymbol{k})\cdot\int\int\int V_{\rm sh}\frac{\partial \boldsymbol{B}}{\partial y}{\rm e}^{-i\boldsymbol{k}\cdot\boldsymbol{x}}{\rm d}^3\boldsymbol{x}\right], \tag{20}$$

$$S = +Re\left[\widetilde{B}^*_y(\boldsymbol{k})\cdot\int\int\int B_x\frac{\partial V_{\rm sh}}{\partial x}{\rm e}^{-i\boldsymbol{k}\cdot\boldsymbol{x}}{\rm d}^3\boldsymbol{x}\right], \tag{21}$$

$$T_{bb} = -Re\left[\widetilde{\boldsymbol{B}}^{\boldsymbol{*}}(\boldsymbol{k})\cdot\int\int\int(\boldsymbol{v}_{\rm t}\cdot\nabla)\boldsymbol{B}{\rm e}^{-i\boldsymbol{k}\cdot\boldsymbol{x}}{\rm d}^3\boldsymbol{x}\right], \tag{22}$$

$$T_{{\rm div}v} = -Re\left[\widetilde{\boldsymbol{B}}^{\boldsymbol{*}}(\boldsymbol{k})\cdot\int\int\int(\nabla\cdot\boldsymbol{v}_{\rm t})\boldsymbol{B}{\rm e}^{-i\boldsymbol{k}\cdot\boldsymbol{x}}{\rm d}^3\boldsymbol{x}\right], \tag{23}$$

$$T_{bv} = +Re\left[\widetilde{\boldsymbol{B}}^{\boldsymbol{*}}(\boldsymbol{k})\cdot\int\int\int(\boldsymbol{B}\cdot\nabla)\boldsymbol{v}_{\rm t}{\rm e}^{-i\boldsymbol{k}\cdot\boldsymbol{x}}{\rm d}^3\boldsymbol{x}\right]. \tag{24}$$

The $D_{\rm mag}$ term has no analytic expression; it is simply what is left over and accounts for numerical losses of magnetic energy (Fromang & Papaloizou 2007). In the present simulations, there is no physical resistivity. The other terms have the following meanings: A is the transfer of magnetic energy between scales by the shear flow, S is the creation of magnetic energy from this shear flow, T_{bb} is the advection of magnetic energy between scales by the turbulent velocity field, $T_{{\rm div}v}$ results from the turbulent compressibility, and T_{bv} describes the creation of magnetic field by the turbulent velocity fluctuations. In each case, Re signifies the real part of the transform.

One can follow a similar procedure using the momentum equation to determine the evolution of the kinetic energy density in Fourier space. As described previously, we include the density in our Fourier transforms. Consider the time derivative of $\sqrt{\rho}\boldsymbol{v}$ given by

$$\frac{\partial\sqrt{\rho}\boldsymbol{v}}{\partial t} = \sqrt{\rho}\frac{\partial\boldsymbol{v}}{\partial t} + \frac{\boldsymbol{v}}{2\sqrt{\rho}}\frac{\partial\rho}{\partial t}. \tag{25}$$

Note that here, for simplicity, we do not decompose the velocity into mean and turbulent components. Using a combination of the continuity and momentum equations, this equation can be written as

$$\begin{aligned}\frac{\partial\sqrt{\rho}\boldsymbol{v}}{\partial t} &= \sqrt{\rho}\left[-\boldsymbol{v}\cdot\nabla\boldsymbol{v} - \frac{1}{\rho}\nabla(P+\frac{1}{2}B^2) + \frac{1}{\rho}(\boldsymbol{B}\cdot\nabla\boldsymbol{B}) - 2\boldsymbol{\Omega}\times\boldsymbol{v} + 2q\Omega^2 x\hat{\boldsymbol{x}}\right] \\ &\quad + \frac{\boldsymbol{v}}{2\sqrt{\rho}}\left[-\rho(\nabla\cdot\boldsymbol{v}) - \boldsymbol{v}\cdot\nabla\rho\right],\end{aligned} \tag{26}$$

If we take the Fourier transform of this equation and dot the result with the complex conjugate of

$$\widetilde{\sqrt{\rho}\boldsymbol{v}}(\boldsymbol{k}) = \int\int\int \sqrt{\rho}(\boldsymbol{x})\boldsymbol{v}(\boldsymbol{x}){\rm e}^{-i\boldsymbol{k}\cdot\boldsymbol{x}}{\rm d}^3\boldsymbol{x}, \tag{27}$$

we arrive at

$$\frac{1}{2}\frac{\partial|\widetilde{\sqrt{\rho}\boldsymbol{v}}(\boldsymbol{k})|^2}{\partial t} = T_{vv} + T_{\rm comp} + T_{vb} + T_{\rm press} + T_{\rm cor} + T_\phi + D_{\rm kin}, \tag{28}$$

where

$$\frac{1}{2}|\widetilde{\sqrt{\rho}\boldsymbol{v}}(\boldsymbol{k})|^2 \equiv \frac{1}{2}\left[|\widetilde{\sqrt{\rho}v_x}(\boldsymbol{k})|^2 + |\widetilde{\sqrt{\rho}v_y}(\boldsymbol{k})|^2 + |\widetilde{\sqrt{\rho}v_z}(\boldsymbol{k})|^2\right], \tag{29}$$

$$T_{vv} = -Re\left[\widetilde{\sqrt{\rho}\boldsymbol{v}^*}(\boldsymbol{k}) \cdot \int\int\int [\sqrt{\rho}(\boldsymbol{v}\cdot\nabla)\boldsymbol{v} + \frac{\boldsymbol{v}}{2\sqrt{\rho}}(\boldsymbol{v}\cdot\nabla)\rho]\mathrm{e}^{-i\boldsymbol{k}\cdot\boldsymbol{x}}\mathrm{d}^3\boldsymbol{x}\right], \tag{30}$$

$$T_{\mathrm{comp}} = -Re\left[\widetilde{\sqrt{\rho}\boldsymbol{v}^*}(\boldsymbol{k}) \cdot \int\int\int \frac{\sqrt{\rho}\boldsymbol{v}}{2}(\nabla\cdot\boldsymbol{v})\mathrm{e}^{-i\boldsymbol{k}\cdot\boldsymbol{x}}\mathrm{d}^3\boldsymbol{x}\right], \tag{31}$$

$$T_{vb} = +Re\left[\widetilde{\sqrt{\rho}\boldsymbol{v}^*}(\boldsymbol{k}) \cdot \int\int\int \frac{1}{\sqrt{\rho}}(\boldsymbol{B}\cdot\nabla)\boldsymbol{B}\mathrm{e}^{-i\boldsymbol{k}\cdot\boldsymbol{x}}\mathrm{d}^3\boldsymbol{x}\right], \tag{32}$$

$$T_{\mathrm{press}} = -Re\left[\widetilde{\sqrt{\rho}\boldsymbol{v}^*}(\boldsymbol{k}) \cdot \int\int\int \frac{1}{\sqrt{\rho}}\nabla(P + \frac{1}{2}B^2)\mathrm{e}^{-i\boldsymbol{k}\cdot\boldsymbol{x}}\mathrm{d}^3\boldsymbol{x}\right], \tag{33}$$

$$T_{\mathrm{cor}} = -Re\left[\widetilde{\sqrt{\rho}\boldsymbol{v}^*}(\boldsymbol{k}) \cdot \int\int\int (2\boldsymbol{\Omega}\times\sqrt{\rho}\boldsymbol{v})\mathrm{e}^{-i\boldsymbol{k}\cdot\boldsymbol{x}}\mathrm{d}^3\boldsymbol{x}\right], \tag{34}$$

$$T_{\phi} = +Re\left[\widetilde{\sqrt{\rho}v_x^*}(\boldsymbol{k}) \cdot \int\int\int 2\sqrt{\rho}q\Omega^2 x\mathrm{e}^{-i\boldsymbol{k}\cdot\boldsymbol{x}}\mathrm{d}^3\boldsymbol{x}\right], \tag{35}$$

and D_{kin} accounts for the dissipation of kinetic energy. Again, this dissipation is numerical as we have not included an explicit viscosity term in our equations. Equation (28) describes the evolution of the kinetic energy density in Fourier space. T_{vv} is a term that describes the transfer of kinetic energy between scales by the velocity field (both the mean and turbulent velocity), T_{comp} results from turbulent compressibility, T_{vb} describes how kinetic energy changes from magnetic tension, T_{press} represents the effect of both gas and magnetic pressure on the kinetic energy, and T_{ϕ} is the effect of the tidal potential on the kinetic energy. Note that T_{cor} is analytically equal to zero, and it is not included in any of the following analysis or discussion.

In the saturated state of the MRI, the magnetic and kinetic energy densities should be in a steady state on average (although they do show strong fluctuations over short periods of time). If we consider the time-averages of equations (19) and (28), then we can set the left hand sides to zero. We then rewrite these equations as

$$T_{vv} + T_{\mathrm{comp}} + T_{vb} + T_{\mathrm{press}} + T_{\phi} + D_{\mathrm{kin}} = 0, \tag{36}$$

$$A + S + T_{bb} + T_{\mathrm{div}v} + T_{bv} + D_{\mathrm{mag}} = 0, \tag{37}$$

where each of these terms is now a time-average. Here we average over 161 snapshots from orbit 20 to 100 in increments of 0.5 orbits. Each of these terms is a function of k_x, k_y, and k_z, and in what follows we average the terms on shells of constant $k = |\boldsymbol{k}|$ as was done in Fromang & Papaloizou (2007).[3] Note that unlike the averaging described in that paper, we include k_y in the calculation of k.

5.1. Zero Net Magnetic Flux

5.1.1. Fiducial Run

In this section, we focus on the Fourier transfer functions for the fiducial zero net magnetic flux simulation. Figure 11 plots the magnetic transfer functions defined in equations (20)-(24) as a function of length scale for SZ128, and Fig. 12 plots the kinetic transfer functions defined in equations (30)-(35). The dashed lines correspond to plus or minus one standard deviation around the mean value of the time average. Most of the transfer functions show large variation at small k values which may be due to poor statistics at small k and relatively large time variability. Because the transfer functions approach zero rapidly, we plot the ranges $1 < kL/(2\pi) < 20$ and $20 < kL/(2\pi) < 64$ in the same figure, but with different y scalings.

The shear term S is positive at all scales, as observed in Fromang & Papaloizou (2007), meaning that B_y is created by the shear flow at all scales. A is small at all scales, supporting the assumption made in Fromang & Papaloizou (2007) that $A \approx 0$. T_{bv} is primarily negative at the largest scales, although there are large fluctuations, and becomes positive for $kL/(2\pi) \gtrsim 35$. The turbulent velocity fluctuations seem to be creating magnetic energy at the smallest scales, but at larger scales, the magnetic field appears to lose energy via this interaction with the turbulence. T_{bb} is negative for k smaller than $kL/(2\pi) \sim 20$, meaning that the turbulence is transferring magnetic energy away from these scales. Although this analysis doesn't determine the direction of this cascade, at the largest scale (i.e., the box size) the energy can only cascade to smaller scales. In terms of absolute value, S and T_{bb} are dominant on the largest scales, while on small scales, $T_{bb} > T_{bv} > S > 0$.

It is difficult to say anything conclusive about the kinetic transfer functions on the largest scales as they are subject to considerable uncertainty, although $T_{vb} < 0$ appears reasonably well constrained at these scales. At smaller scales, the two dominant terms are T_{vv} and T_{vb}, with $T_{vb} > T_{vv} > 0$; kinetic energy is being transferred to these scales by the

[3]In our analysis, the average over shells of constant k was done before the temporal average.

turbulence, and being created by magnetic field.

Equations (36) and (37) have been set to zero from the assumption that the magnetic and kinetic energies are in a time-averaged steady state. The dissipation terms $D_{\rm mag}$ and $D_{\rm kin}$ are simply what is left over after the other transfer functions have been computed. The top plots in Fig. 13 are the kinetic and magnetic dissipation and the ratio $D_{\rm kin}/D_{\rm mag}$ as a function of k for $20 < kL/(2\pi) < 64$; the scatter at small k is large and there is considerable uncertainty in the dissipation values. At small scales, magnetic dissipation dominates kinetic dissipation by a factor of roughly three. The kinetic and magnetic dissipation rate increases in magnitude towards larger scales.

Following Fromang & Papaloizou (2007), we can determine an effective resistivity and viscosity as a function of length scale by assuming that the numerical effects behave as if they were physical resistivity and viscosity. For example, with a constant Ohmic resistivity, the induction equation would have an additional term proportional to $\nabla^2 B$, with the constant of proportionality being the resistivity. If we take the Fourier transform of this term and dot it with the complex conjugate of $\widetilde{\boldsymbol{B}}(\boldsymbol{k})$, the real part is

$$T_\eta = +Re\left[\widetilde{\boldsymbol{B}}^{\boldsymbol{*}}(\boldsymbol{k}) \cdot \int\int\int \nabla^2 \boldsymbol{B} \mathrm{e}^{-i\boldsymbol{k}\cdot\boldsymbol{x}} \mathrm{d}^3\boldsymbol{x}\right] = -k^2 |\widetilde{\boldsymbol{B}}(\boldsymbol{k})|^2. \tag{38}$$

We can then define an effective resistivity as a function of k by

$$\eta_{\rm eff}(k) \equiv \frac{D_{\rm mag}(k)}{T_\eta(k)}. \tag{39}$$

Similarly, a constant kinematic shear viscosity would add a term proportional to $\sqrt{\rho}[\nabla^2\boldsymbol{v} + \frac{1}{3}\nabla(\nabla\cdot\boldsymbol{v})]$ to equation (26), with the constant of proportionality being the viscosity. Note that we only consider shear viscosity here for simplicity. We take the Fourier transform of the viscous term, dot it with the complex conjugate of equation (27), and take the real part. The result is

$$T_\nu = +Re\left[\widetilde{\sqrt{\rho}\boldsymbol{v}^{\boldsymbol{*}}}(\boldsymbol{k}) \cdot \int\int\int \sqrt{\rho}[\nabla^2\boldsymbol{v} + \frac{1}{3}\nabla(\nabla\cdot\boldsymbol{v})] \mathrm{e}^{-i\boldsymbol{k}\cdot\boldsymbol{x}} \mathrm{d}^3\boldsymbol{x}\right]. \tag{40}$$

This equation can be made simpler by realizing that the second term of the integrand, related to the divergence of $\boldsymbol{v}$, is negligible. We can also assume that the density is relatively constant, and arrive at

$$T_\nu = -k^2 |\widetilde{\sqrt{\rho}\boldsymbol{\delta v}}(\boldsymbol{k})|^2. \tag{41}$$

We have substituted the perturbed velocity here because it is the only velocity that can lead to *numerical* dissipation of kinetic energy. That is, a pure shear flow will not encounter any numerical viscosity, and we can subtract off this flow. We define an effective viscosity by

$$\nu_{\rm eff}(k) \equiv \frac{D_{\rm kin}(k)}{T_\nu(k)}. \tag{42}$$

We can also characterize the effective resistivity and viscosity in terms of a Reynolds number,

$$Re_{\rm eff}(k) \equiv \frac{c_o H}{\nu_{\rm eff}(k)}, \tag{43}$$

and magnetic Reynolds number,

$$Rm_{\rm eff}(k) \equiv \frac{c_o H}{\eta_{\rm eff}(k)}, \tag{44}$$

where we have used the initial isothermal sound speed, $c_o = 0.001$, as a characteristic velocity, and $H = L_z$ is a characteristic length. These numbers quantify the numerical dissipation coefficients in a dimensionless manner.

Finally, we define an effective Prandtl number by

$$P_{m,\rm eff}(k) \equiv \frac{\nu_{\rm eff}(k)}{\eta_{\rm eff}(k)} \tag{45}$$

The effective viscosity and resistivity as well as the effective Prandtl number are shown in the bottom plots of Fig. 13. The viscosity and resistivity are fairly constant at large k. The effective Reynolds numbers are on the order of $Re_{\rm eff} \sim 12000$, and $Rm_{\rm eff} \sim 20000$ at large k. The Prandtl number is also relatively flat at these scales, and $P_{m,\rm eff} \sim 1.6$. This result agrees with Fromang & Papaloizou (2007), where $P_{m,\rm eff} > 1$ for ZEUS. While the numerical dissipation of Athena is not physical, the "flatness" of $\nu_{\rm eff}$ and $\eta_{\rm eff}$ suggests a resemblance to physical dissipation at small scales.

Finally, note that although the Prandtl number is greater than unity, the magnetic dissipation dominates over kinetic dissipation. Evidently, T_η is larger than T_ν because there is more magnetic energy than kinetic energy at a given scale. In particular,

$$\frac{T_\eta}{T_\nu} = \frac{|\widetilde{\boldsymbol{B}}(\boldsymbol{k})|^2}{|\widetilde{\sqrt{\rho}\boldsymbol{\delta v}}(\boldsymbol{k})|^2}. \tag{46}$$

Since there is more magnetic energy than perturbed kinetic energy at a given scale, magnetic dissipation dominates.

5.1.2. Resolution Effects

To gauge the effect of resolution on these various quantities, we perform the same analysis on the lower resolution runs, SZ16, SZ32, and SZ64. We focus, in particular, on the small scales (i.e., large k) where our quantities are statistically more well-determined. Figure 14 shows $\nu_{\rm eff}$, $\eta_{\rm eff}$, $P_{m,{\rm eff}}$, and the ratio of $D_{\rm kin}$ to $D_{\rm mag}$ as a function of x resolution, N_x. The data points are calculated by averaging the quantity of interest over k in the regions of k-space where the error on the quantity is less than its mean value.[4] The displayed error bars are the propagation of the errors from the temporal statistics. At these large values of k, $\nu_{\rm eff}$, $\eta_{\rm eff}$, $P_{m,{\rm eff}}$, and $D_{\rm kin}/D_{\rm mag}$ are relatively flat, varying by a factor of at most 2. Consequently, these averages should be representative at small scales.

The numerical viscosity and resistivity decrease as a function of resolution. The dashed lines in the two upper panels of the figure show the line $\nu_{\rm eff}, \eta_{\rm eff} \propto N_x^{-2}$. The viscosity and resistivity decrease slower than this with increasing N_x; we measured $\nu_{\rm eff}, \eta_{\rm eff} \propto N_x^{-1.6}$. The figure also shows that both the effective Prandtl number and the ratio of kinetic to magnetic dissipation are constant with resolution to within the error bars.

5.1.3. Comparison with Previous Results

Fromang & Papaloizou (2007) were interested in the transfer function for the poloidal field, as the regeneration of this field is key to a self-sustaining dynamo. They found that the magnetic dissipation of ZEUS for the poloidal magnetic field departs from the physical dissipation model at small k and could even be a nonphysical "positive" dissipation. We repeat the same analysis as performed in that paper, but with SZ128, for comparison. First, we examine the magnetic dissipation for the full 3D Fourier analysis described above. Second, we do the same procedure but setting $B_y = 0$ to focus on the effect of only including

[4]There are some quantities for which the error is never less than the mean. In these cases, we average over regions where the mean is greater than 80% of the error.

poloidal field. Finally, we perform the procedure with $B_y = 0$ and in the plane $k_y = 0$ (i.e., axisymmetry). These simplifications allow us to reproduce the poloidal field analysis of Fromang & Papaloizou (2007).

The results are shown in Fig. 15. The left two plots correspond to the Fourier analysis in which only $B_y = 0$ is assumed. The right plots assume $B_y = 0$ and $k_y = 0$. The black lines in the bottom two plots correspond to the magnetic dissipation for the full 3D Fourier analysis with $B_y \neq 0$ and $k_y \neq 0$. It is apparent that when $B_y = 0$ is assumed in the calculations, the magnetic dissipation becomes positive at large scales. However, when B_y is included, the magnetic dissipation remains negative. Whether or not $k_y = 0$ is assumed seems to make very little difference, supporting the notion that small k_y dominates. Since Athena and ZEUS both find positive $D_{\rm mag}$ at small k, it is unlikely that this effect can be attributed to algorithmic limitations specific to ZEUS. Since $D_{\rm mag}$ is not a derived quantity but simply what remains after all the transfer functions are calculated, it seems likely that the positive $D_{\rm mag}$ values for the poloidal field analysis are due to incomplete statistics at large scales, or other inadequacies of the analysis when applied solely to the poloidal field. At small k, the standard deviations of the quantities (dashed lines) are considerable. The standard deviation on $D_{\rm mag}$ when $B_y \neq 0$ is significantly larger than when one sets $B_y = 0$. This reflects the large variability of $\langle B_y^2/2 \rangle$ compared to the other components of magnetic energy (see e.g., Fig. 2). At any given time, $D_{\rm mag}$ can be positive; the assumption of time-stationarity does not hold at any point in time. But when the data are time-averaged, $D_{\rm mag} < 0$.

Finally, we compare the numerical magnetic Reyolds number calculated with equation (44) but with the $B_y = 0$ and $k_y = 0$ assumptions. For SZ128, we find that $Rm_{\rm eff} \sim 11000$, and for SZ64, $Rm_{\rm eff} \sim 3500$. Fromang & Papaloizou (2007) find $Rm_{\rm eff} \sim 30000$ for their $N_x = 128$ run, and $Rm_{\rm eff} \sim 10000$ for their $N_x = 64$ run; both of their calculated effective Reynolds numbers are larger than those calculated for Athena. This result seems to suggest that ZEUS is actually less dissipative than Athena. However, there are several points to consider. First, numerical dissipation is a nonlinear function of resolution, sharply increasing as the number of zones per wavelength decreases (high wavenumbers). The effective Reynolds number is obtained by measuring dissipation at the high k end of the spectrum. As reported by Shen, Stone, & Gardiner (2006) Athena appears to have higher dissipation than ZEUS for poorly resolved waves, as evidenced by the ability of Athena to avoid the aliasing errors seen with ZEUS for hydrodynamic shearing box waves. They further point out that for wavelengths larger than 16 grid points Athena is less dissipative. Further, 2D simulations of decaying turbulence have demonstrated that when saturation amplitude is reached, the decay time is longer in Athena than in ZEUS, consistent with Athena having a higher effective resolution (Stone & Gardiner 2005). In the present context, we find that the time- and volume-averaged total stresses in our simulations are larger than those calculated

in the simulations of Fromang & Papaloizou (2007). Stronger turbulence leads to larger kinetic and magnetic turbulent fluctuations, which in turn enhances dissipation via grid-scale effects. Finally, we reemphasize that assuming $B_y = 0$ may have a significant impact on the measurement of effective magnetic dissipation via this analysis.

5.2. Net Magnetic Flux

5.2.1. Fiducial Run

We perform the same transfer function analysis on the fiducial net magnetic flux run, NZ128. The various transfer function terms as a function of k are shown in Figs. 16–17. As was the case in the zero net flux simulation, S is positive at all scales and dominates at small k; A is relatively small throughout. T_{bv} and T_{bb} are negative at large scales and positive at small scales, with $T_{bb} > 0$ for $kL/(2\pi) \gtrsim 5$, and $T_{bv} > 0$ for $kL/(2\pi) \gtrsim 20$. At small scales, $T_{bb} > T_{bv} > S > 0$. Of the kinetic terms, T_{vv} and T_{vb} dominate with $T_{vb} > T_{vv} > 0$. These results are in general agreement with SZ128, except that the magnitude of the various terms is larger for NZ128 than for SZ128, and T_{bb} and T_{bv} become positive at smaller k values compared to SZ128.

As before, we calculate the kinetic and magnetic dissipation as well as effective values for the viscosity and resistivity. Figure 18 shows these quantities for NZ128 at the smallest scales. As was the case for SZ128, the mean magnetic dissipation dominates over kinetic dissipation by a factor of roughly three at these scales. Note, however, the large error bars associated with these plots, which encompass values of $D_{\rm kin}/D_{\rm mag} > 1$. Again, the error bars are the temporal standard deviation of the transfer functions. Since NZ128 has a larger temporal variability, larger error bars are expected. The mean value for $D_{\rm kin}/D_{\rm mag}$ is on the order of 0.6-0.7, which is consistent with the analysis in § 4.1 in which we found $\dot{Q}_{\rm k}/\dot{Q}_{\rm m} \sim 0.6$.

The effective viscosity and resistivity show the same basic result as in the SZ128 case. $\nu_{\rm eff}$, $\eta_{\rm eff}$, and $P_{m,\rm eff}$ change by a factor of order unity at large k. The effective Reynolds numbers are on the order of $Re_{\rm eff} \sim 4000$, and $Rm_{\rm eff} \sim 8000$ at large k. $P_{m,\rm eff}$ has a mean value of ~ 1.9. Again, there is considerable uncertainty in these values due to the large amplitude fluctuations in the turbulence. The error bars encompass values of $P_{m,\rm eff}$ less than unity. As a result, it is more difficult to conclusively say that the dissipation behaves the same way in NZ128 as in SZ128. However, in an average sense, the two simulations agree well qualitatively.

5.2.2. Resolution Effects

We can again look at the effect of resolution on these various dissipation quantities. Figure 19 shows this effect for the net flux simulations (NZ16, NZ32, NZ64, and NZ128). The procedure by which to average over k is the same as described in § 5.1.2. The displayed error bars are the propagation of the errors from the temporal statistics. At these large values of k, $\nu_{\rm eff}$, $\eta_{\rm eff}$, $P_{m,{\rm eff}}$, and $D_{\rm kin}/D_{\rm mag}$ are relatively flat, varying by a factor of at most 2.

The numerical viscosity and resistivity decrease as a function of resolution. The dashed lines in the two upper panels of the figure show the line $\nu_{\rm eff}, \eta_{\rm eff} \propto N_x^{-2}$. The viscosity and resistivity decrease slower than this with increasing N_x; we measured $\nu_{\rm eff}, \eta_{\rm eff} \propto N_x^{-1.3}$. The figure shows that the effective Prandtl number is constant with resolution to within the error bars. There appears to be a slight increase in $D_{\rm kin}/D_{\rm mag}$ with resolution, but this trend is not definitive given the large uncertainties on the data.

One might expect $\nu_{\rm eff}$ and $\eta_{\rm eff}$ to decrease with increasing resolution since these terms arise from truncation error. Linear wave advection test problems with Athena have shown that the truncation error converges at second order (e.g., Stone et al. 2008). On this basis, one would expect $\nu_{\rm eff}, \eta_{\rm eff} \propto N_x^{-2}$. We find a shallower decrease with N_x, but MRI turbulence is a fully nonlinear system, and one should not necessarily expect the same convergence behavior as in a linear system.

6. Discussion and Conclusions

We have carried out a series of local, unstratified shearing box simulations with the recently developed Athena code to study the characteristics of MRI driven turbulence. Athena uses a second-order, conservative, compressive MHD algorithm, which is significantly different from the algorithms employed in many of the previous MRI studies. In our work, we have run several standard models for comparison with previous work, and characterized the numerical dissipation of the Athena code for the shearing box problem. Furthermore, we have exploited the energy conservation property of Athena to carry out a study of energy flow within MRI-driven turbulence.

To compare with previous numerical results, we have investigated the effects of different initial field geometries (uniform or sinusoidal B_z), varying domain aspect ratio, and numerical resolution. In all of our simulations, the MRI is initiated and sustained over many orbits. The time- and volume-averaged properties of the resulting turbulent flow, such as stress levels and magnetic and kinetic energies, are consistent with previous results. As in previous

work, we find that boxes containing net vertical field saturate at higher amplitudes compared to those without net fields. The total stress is proportional to the magnetic pressure with a constant of proportionality ~ 0.5, but is independent of the gas pressure. In the net field simulation, the gas pressure increases by a factor of 100, due to thermalization of the turbulence, without affecting the stress. The consistency of these results with past work indicate that these properties do not result from details of the employed algorithm.

Fourier analysis of the turbulence shows that the largest scales in the box dominate the energetics. In the presence of a net field, the amplitude of the spatial power spectra is largely independent of resolution on the largest scales. This is not true for the zero net flux simulations however. For those simulations, the amplitude decreases as resolution increases, which is consistent with the overall resolution behavior. For net field simulations, the averaged turbulent magnetic and kinetic energies increase slightly with resolution, whereas for the zero net field simulations, the energies decrease with increasing resolution roughly in proportion to the grid zone size. This apparent lack of convergence for the zero net field shearing box simulations was previously demonstrated by Fromang & Papaloizou (2007) using the ZEUS code.

The net field simulation shows intermittent channel flows which cause temporary increases in stress through amplification of large-scale MRI modes. The parasitic modes described by Goodman & Xu (1994) destroy the channel flow within about one orbit of time, but the rapid increase in stress produces a subsequent increase in thermal energy. The presence of these discrete channel flow events is a consequence of the box size—larger boxes do not experience them—but we use their presence to study the subsequent energy flow following a rapid increase in stress.

Because Athena evolves the total energy equation, magnetic and kinetic energy losses due to numerical grid-scale effects are added to the internal energy. This makes Athena well suited to examining the turbulent energy flow and subsequent dissipation. The recurring channel flows in the net flux model provide a sudden injection of energy into the box by increasing the stress operating on the shearing boundaries of the box. The injected energy appears as heat after ~ 0.2 orbits. This corresponds to a timescale Ω^{-1}, which equals $L_z/c_{\rm s}$ where $c_{\rm s}$ is the initial soundspeed. This timescale determines the amplitude of the Alfvén speed, $v_{\rm A}$, and its fundamental MRI wavelength, $\lambda_{\rm MRI}$; $L_z/c_{\rm s} \sim \lambda_{\rm MRI}/v_{\rm A}$. The timescale is thus on the order of the eddy turnover time, indicating that dissipational heating is a local process and that energy is not carried over large distances before it is thermalized.

In the fiducial zero net magnetic flux simulation, SZ128, there are no recurring channel modes, making it more difficult to trace the flow of injected energy. The analysis is further complicated by the presence of compressive waves that dominate the time derivative of the

thermal energy, $\dot{T}$. These waves are also present in the net field simulations, but their amplitude is smaller relative to the larger turbulent kinetic energy found with a net field. A detailed examination of the components of the internal energy equation indicate that the compressive waves do not appear to contribute significantly to irreversible heating. By averaging $\dot{T}$ for the zero net flux simulation, we find a correlation of $\dot{T}$ with $E_{\rm in}$ on the same timescale of ~ 0.2 orbits.

In the net field simulation, the dissipation of magnetic energy is larger than that for the kinetic energy, not unexpected as the ratio of the average magnetic to perturbed kinetic energy is ~ 3.4. But the ratio of the magnetic to kinetic dissipation rate is roughly constant at ~ 1.7. The fact that the ratio of dissipation rates does not equal the ratio of energies may result from a couple of possibilities. First, there could be a net transfer of magnetic to *perturbed* kinetic energy as was suggested in Brandenburg et al. (1995).[5] Second, the difference in the ratios could arise from the effective Prandtl number being larger than one. In particular, if $\dot{Q}_{\rm k} \propto \nu_{\rm eff}\delta v^2/2$ and $\dot{Q}_{\rm m} \propto \eta_{\rm eff}B^2/2$, then $(B^2/\delta v^2)(\dot{Q}_{\rm k}/\dot{Q}_{\rm m}) \sim P_{m,{\rm eff}}$. With the above values for the energy and dissipation ratios, we find $(B^2/\delta v^2)(\dot{Q}_{\rm k}/\dot{Q}_{\rm m}) \sim 2$, which is consistent with the determination of $P_{m,{\rm eff}}$ from the Fourier analysis (see discussion below). The agreement between the two separate calculations of $P_{m,{\rm eff}}$ may be coincidental, but it is suggestive of $\dot{Q}_{\rm k} \propto \nu_{\rm eff}\delta v^2/2$ and $\dot{Q}_{\rm m} \propto \eta_{\rm eff}B^2/2$.

The turbulence is sustained by the continued action of the MRI in extracting energy from the differential rotation. This can be removed from the simulations allowing us to study the decay of the turbulence in detail (simulations NZD128 and SZD128). Figure 10 shows that magnetic losses dominate over kinetic losses during this decay. In both simulations nearly 50% of the magnetic energy and 20% of the kinetic energy has been dissipated after 0.2 orbits. By one orbit into the decay, most of the magnetic and kinetic energy has been lost. Although these decay timescales arise in a turbulent flow that lacks power input from the MRI, the results are consistent with the conclusion that turbulent energy dissipation occurs on a rapid timescale of order Ω^{-1}.

Fromang & Papaloizou (2007) used a detailed Fourier analysis (§ 5) to study magnetic energy flow and thermalization as a function of length scale in the shearing box. In this analysis, the individual terms in the evolution equation for the magnetic energy are examined in Fourier space. Averaging over time and assuming that the magnetic energy is in a statistical steady state, one sets the sum of these terms equal to a remainder, which is

[5]§ 4.1 shows that there is in fact a net transfer of kinetic to magnetic energy. However, this kinetic energy includes the shear flow, and thus, this result tells us nothing of the energy transfer between magnetic and *perturbed* kinetic energy.

credited to numerical effects. These numerical losses can then be modeled as an effective resistivity (and viscosity for the kinetic energy), allowing one to characterize the numerical dissipation in the simulation.

We repeated their analysis with Athena and extended it to the kinetic energy. The dominant effect at large scales is the generation of magnetic field by the background shear. This energy is transferred to other scales by the turbulence. Net positive field creation by the turbulent flow and energy gains by the transfer between scales only happens at small wavelengths. This point of transition from loss to gain happens at smaller scales for the zero net field simulation compared to the net field model. Magnetic dissipation dominates over kinetic dissipation at small scales (i.e., $kL/(2\pi) \gtrsim 20$). Modeling these as an effective resistivity η and viscosity ν shows that η and ν drop with increasing resolution with a power that lies between first- and second-order in grid resolution. The effective Prandtl number, on the other hand, is nearly constant as a function of resolution with a value between ~ 1.5 and 2.

Fromang & Papaloizou (2007) observed what they described as "negative" resistivity in an analysis restricted to the poloidal field alone. In repeating their exact analysis with Athena, we also observed such an "anti-dissipation" at large scales. This indicates that this effect is not associated with a numerical algorithm limitation associated with ZEUS. More likely, it arises from the statistical uncertainty at large scales and from the failure of the assumptions that go into the definition of the dissipation term. We note that the inclusion of the toroidal field B_y in the analysis shows net dissipation at all scales, although again the statistical variation is large at large scales.

In conclusion, what do these results imply for shearing box simulations and the MRI? First, as observed by Fromang & Papaloizou (2007), the scales over which turbulent energy generation occurs are not well-separated from those where there is significant dissipation; the MRI operates over a wide range of scales. The MRI grows at a rate $\sim kv_{\rm A}$ for all k less than $\Omega/v_{\rm A}$. At large scales, a weak field will grow more slowly than the timescale over which energy is transferred between scales, between magnetic and kinetic forms, and ultimately thermalized. If a field is chopped up by reconnection, it may be reduced to small scales where the MRI no longer operates. In the presence of a net field, there will always be a significant driving term at the scales set by that imposed field. In the absence of such a field, however, the outcome will be determined by the complex interplay of loss due to dissipation and amplification by the MRI. In the numerical simulations with zero net field, increasing the resolution causes an overall decrease in the saturation energies. Fromang & Papaloizou (2007) attribute this to higher resolution enabling the MRI to operate at intermediate scales which facilitates the transfer of energy to small scales and promotes

reconnection and dissipation. What is perhaps surprising is that resolving the MRI at these scales leads to greater field dissipation than would otherwise be accomplished by the numerical losses that would occur if those scales were underresolved. Because the same effect is observed with both Athena and ZEUS, it seems likely that this ability of the MRI to transfer energy away from the largest scales in the shearing box and to increase the total dissipation is a physical rather than numerical effect.

In related work, Fromang et al. (2007) and Lesur & Longaretti (2007) studied the effect of varying the physical (not numerical) magnetic Prandtl number, P_m, on the turbulence. They found that the saturation amplitudes were increased with increased P_m. Fromang et al. (2007) found evidence that there exists a critical $P_m > 1$ below which zero net field simulations would die out rather than achieve a steady turbulent state. Our results in this investigation show that this Prandtl number dependence is a distinct effect from the observed dependence of the turbulence on resolution. We find the numerical P_m to be largely independent of resolution in Athena. Taken together, however, the dependence on physical P_m and the dependence on resolution point to the importance of small and intermediate scale magnetic dissipation and reconnection to establishing saturation amplitudes in MRI-driven turbulence.

As discussed by Fromang & Papaloizou (2007), numerical dissipation can deviate significantly from physical dissipation. In § 5.1.1, we showed that $\eta_{\rm eff}$ and $\nu_{\rm eff}$ are relatively flat at small scales, suggesting a resemblance to physical dissipation. However, consider the numerical Reynolds number as calculated from equation (43) for our zero net flux simulations. For $N_x = 128$, we found $Re_{\rm eff} \sim 12000$, and $P_{m,{\rm eff}} \sim 1.6$ for all of zero net flux simulations. From the parameter space studies of Fromang et al. (2007), these values for the Reynolds and Prandtl numbers correspond to marginal MRI turublence; that is, they lie very close to the critical line between sustained and decaying turbulence. For $N_x = 64$, $Re_{\rm eff} \sim 4100$, and the Reynolds number is even smaller for the lower resolutions. These values are well within the decaying turbulence regime, but we find active MRI turbulence in all of our simulations. These results show that the effective Reynolds and Prandtl numbers of Athena as measured at large wavenumbers does not apply at smaller k values where there are many grid zones per wavelength. Thus, the Reynolds numbers and Prandtl numbers that we calculate should be taken as a measure of the effective numerical dissipation of the code and not equated to a flow with the same Reynolds and Prandtl number as determined by a simple physical resistivity and viscosity.

This result highlights an uncertainty associated with any MRI simulation that depends only on numerical rather than physical dissipation. It is apparent that the numerical Prandtl number can play an important role in determining the ratio of magnetic to kinetic dissipation.

More speculatively, the Prandtl number may also play a role in the timescale over which thermalization occurs. In the present study, we found that both the thermalization timescale and the effective numerical Prandtl number were largely independent of resolution. However, the turbulent energy thermalization timescales and properties we measure may be subject to change when explicit dissipation is included. It will be a very important next step in this work to include physical dissipation and verify these results.

This work is only the first step in applying Athena to the problem of the energetics of MRI turbulence. The present study provides a calibration of the numerical dissipation, which will be important in future studies that include explicit resistivity and viscosity. Furthermore, the unstratified shearing box has the virtue of simplicity and allows a detailed study of MRI turbulence without too many confounding factors, but it also may prove too limited for predictive application to accretion flows. The inclusion of vertical stratification and radiative cooling are both straightforward extensions to the present study. The detailed diagnostics developed and applied in this study should prove valuable in this planned work.

We thank Jim Stone, Steve Balbus, and Sebastien Fromang for useful discussions and suggestions regarding this work. We also thank the anonymous referee whose comments and suggestions improved this paper. This material is based upon work supported by NASA Grants NNG04GK77G and NAG5-13288. The simulations were run on the NCSA Tera-Grid IA-64 Linux Cluster (Mercury) and the University of Virginia Astronomy Department Beowulf Cluster.

REFERENCES

Balbus, S. A., & Hawley, J. F. 1991, ApJ, 376, 214

—. 1998, Reviews of Modern Physics, 70, 1

Balbus, S. A., & Papaloizou, J. C. B. 1999, ApJ, 521, 650

Beckwith, K., Hawley, J. F., & Krolik, J. H. 2008, MNRAS, 1003

Blackman, E. G., Penna, R. F., & Varnière, P. 2008, New Astronomy, 13, 244

Blaes, O., Hirose, S., & Krolik, J. H. 2007, ApJ, 664, 1057

Bodo, G., Mignone, A., Cattaneo, F., Rossi, P., & Ferrari, A. 2008, A&A, 487, 1

Brandenburg, A., Nordlund, A., Stein, R. F., & Torkelsson, U. 1995, ApJ, 446, 741

Colella, P., & Woodward, P. R. 1984, Journal of Computational Physics, 54, 174

Colella, P. 1990, Journal of Computational Physics, 87, 171

Fleming, T. P., Stone, J. M., & Hawley, J. F. 2000, ApJ, 530, 464

Fromang, S., & Papaloizou, J. 2007, A&A, 476, 1113

Fromang, S., Papaloizou, J., Lesur, G., & Heinemann, T. 2007, A&A, 476, 1123

Gardiner, T. A., & Stone, J. M. 2005a, Journal of Computational Physics, 205, 509

Gardiner, T. A., & Stone, J. M. 2005b, in American Institute of Physics Conference Series, Vol. 784, Magnetic Fields in the Universe: From Laboratory and Stars to Primordial Structures., ed. E. M. de Gouveia dal Pino, G. Lugones, & A. Lazarian, 475–488

—. 2008, Journal of Computational Physics, 227, 4123

Goodman, J., & Xu, G. 1994, ApJ, 432, 213

Hawley, J. F., & Balbus, S. A. 1992, ApJ, 400, 595

Hawley, J. F., Gammie, C. F., & Balbus, S. A. 1995, ApJ, 440, 742

—. 1996, ApJ, 464, 690

Hirose, S., Krolik, J. H., & Stone, J. M. 2006, ApJ, 640, 901

Krolik, J. H., Hirose, S., & Blaes, O. 2007, ApJ, 664, 1045

Lesur, G., & Longaretti, P.-Y. 2007, MNRAS, 378, 1471

Pessah, M. E., Chan, C.-k., & Psaltis, D. 2007, ApJ, 668, L51

Sano, T., & Inutsuka, S.-i. 2001, ApJ, 561, L179

Sano, T., Inutsuka, S.-I., & Miyama, S. M. 1998, ApJ, 506, L57

Sano, T., Inutsuka, S.-i., Turner, N. J., & Stone, J. M. 2004, ApJ, 605, 321

Sano, T., & Stone, J. M. 2002, ApJ, 577, 534

Shakura, N. I., & Syunyaev, R. A. 1973, A&A, 24, 337

Shen, Y., Stone, J. M. & Gardiner, T. A. 2006, ApJ, 653, 513

Stone, J. M., & Gardiner, T. A. 2005, in American Institute of Physics Conference Series, Vol. 784, Magnetic Fields in the Universe: From Laboratory and Stars to Primordial Structures., ed. E. M. de Gouveia dal Pino, G. Lugones, & A. Lazarian, 16–26

Stone, J. M., Gardiner, T. A., Teuben, P., Hawley, J. F., & Simon, J. B. 2008, ApJS, 178, 137

Stone, J. M., Hawley, J. F., Gammie, C. F., & Balbus, S. A. 1996, ApJ, 463, 656

Stone, J. M., & Norman, M. L. 1992a, ApJS, 80, 753

—. 1992b, ApJS, 80, 791

Ziegler, U., & Rüdiger, G. 2001, A&A, 378, 668

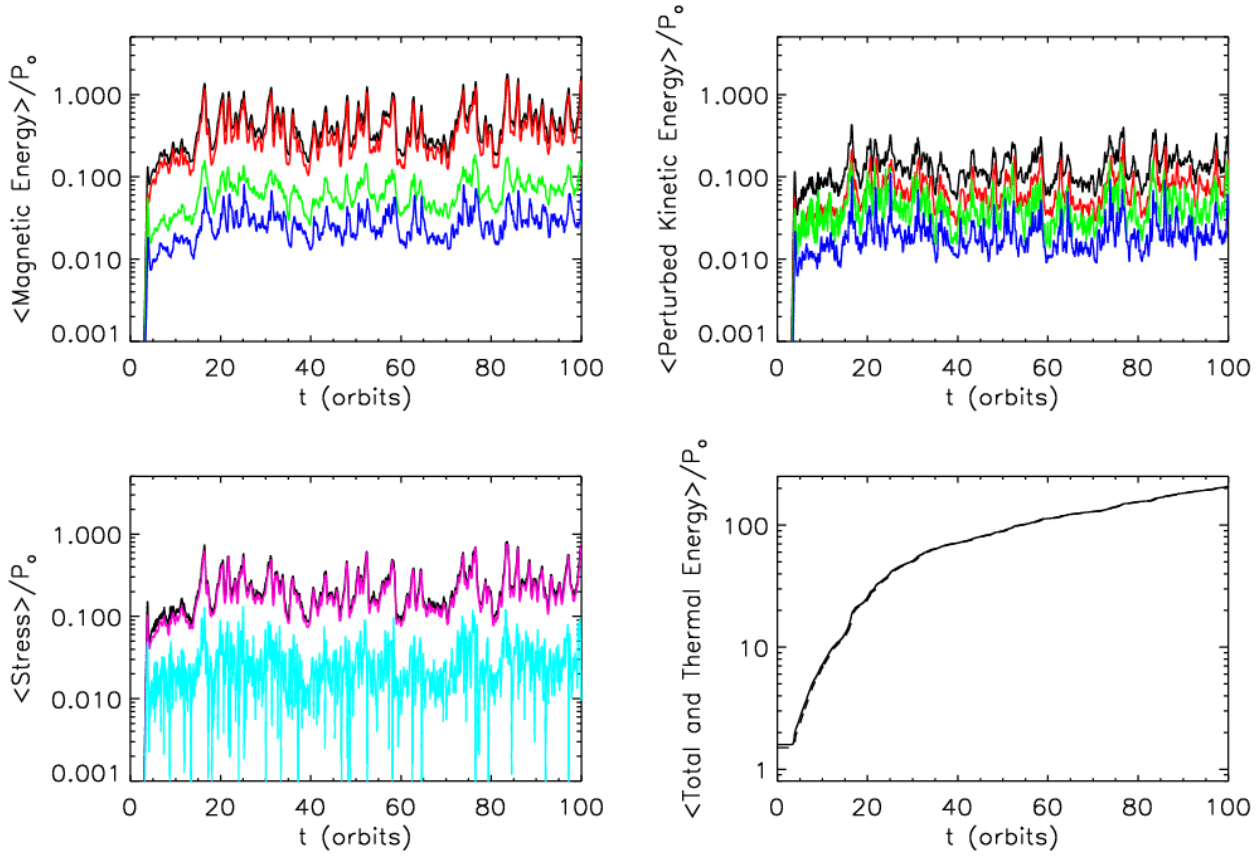

Fig. 1.— Volume-averaged energy densities and stresses normalized to the initial gas pressure versus time for the NZ128 simulation. In the upper two plots, the black line is the total energy density, the green line is the component of the energy density in the x direction, the red line is the y direction component, and the blue line is the z direction component. The upper left plot shows the volume-averaged magnetic energy density, the upper right plot shows the perturbed kinetic energy density (i.e., with the shear subtracted off of v_y), and the lower left plot is the volume-averaged total stress (black), Maxwell stress (pink), and Reynolds stress (blue). The lower right plot is the total energy density, including gravitational energy (solid line), and the thermal energy density (dashed line). The y axes have the same range for all plots except for the total/thermal energy density plot.

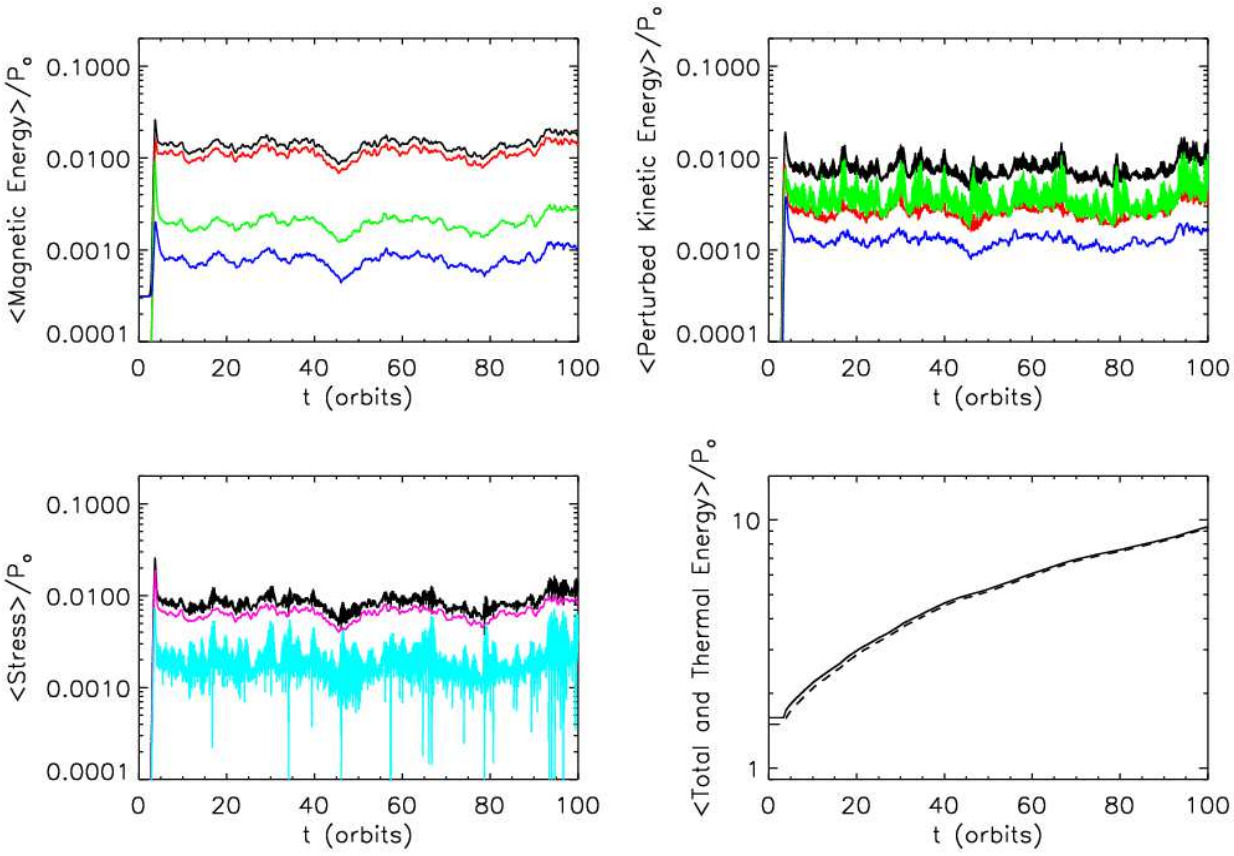

Fig. 2.— Volume-averaged energy densities and stresses normalized to the initial gas pressure versus time for the SZ128 simulation. In the upper two plots, the black line is the total energy density, the green line is the component of the energy density in the x direction, the red line is the y direction component, and the blue line is the z direction component. The upper left plot shows the volume-averaged magnetic energy density, the upper right plot shows the perturbed kinetic energy density (i.e., with the shear subtracted off of v_y), and the lower left plot is the volume-averaged total stress (black), Maxwell stress (pink), and Reynolds stress (blue). The lower right plot is the total energy density, including gravitational energy (solid line), and the thermal energy density (dashed line). The y axes have the same range for all plots except for the total/thermal energy density plot.

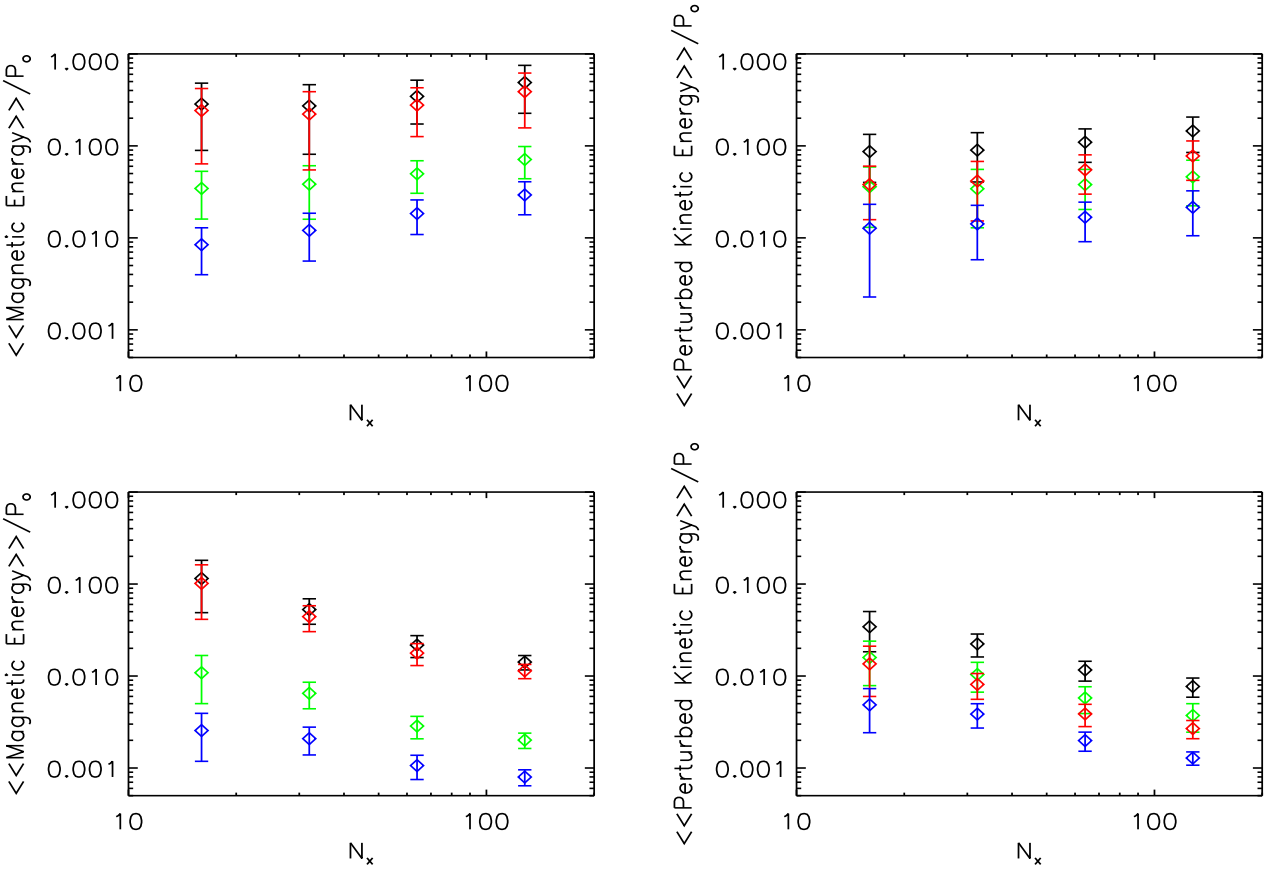

Fig. 3.— Time- and volume-averaged energy densities normalized to the initial pressure for various resolutions. The two upper plots correspond to the net flux simulations, and the two lower plots correspond to the zero net flux simulations. The left plots are the averaged magnetic energy densities, and the right plots are the averaged perturbed kinetic energy densities (i.e., with shear subtracted off of v_y). In all plots, the black symbols are the total energy density, the green symbols are the x component of the energy density, the red symbols are the y component, and the blue symbols are the z component. The time averages are done from orbit 20 to 100, and the error bars indicate one standard deviation over this period.

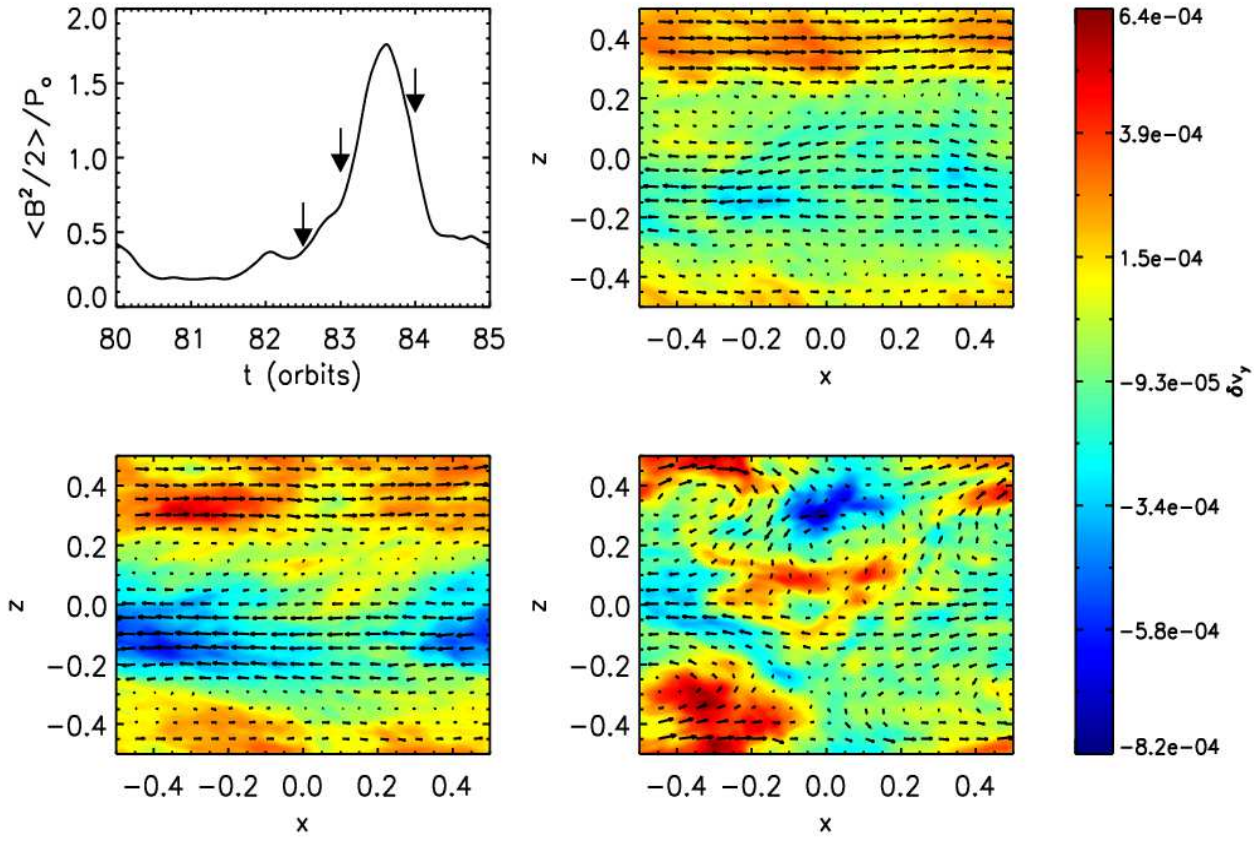

Fig. 4.— The development and destruction of a channel flow during the NZ128 simulation. The upper left plot shows a fluctuation in the volume-averaged magnetic energy density from $t = 80$ orbits to $t = 85$ orbits. The remaining plots show the y-averaged perturbed y velocity (colors) and v_x and v_z (vectors). The upper right plot occurs at $t = 82.5$ orbits, the lower left plot occurs at $t = 83$ orbits, and the lower right plot occurs at $t = 84$ orbits. These times are indicated on the upper left plot by the arrows. At $t = 82.5$ orbits, one can see the development of a two-channel flow, in which one channel has $v_x < 0$ and $\delta v_y < 0$, and the other channel has $v_x > 0$ and $\delta v_y > 0$. At $t = 83$ orbits, this channel flow is even more developed as the perturbations to the y velocity have become even stronger and v_x dominates over v_z everywhere. The development of this channel flow coincides with an increase in volume-averaged magnetic energy density. By $t = 84$ orbits, the channel flow has been destroyed, coinciding with the decrease in magnetic energy density.

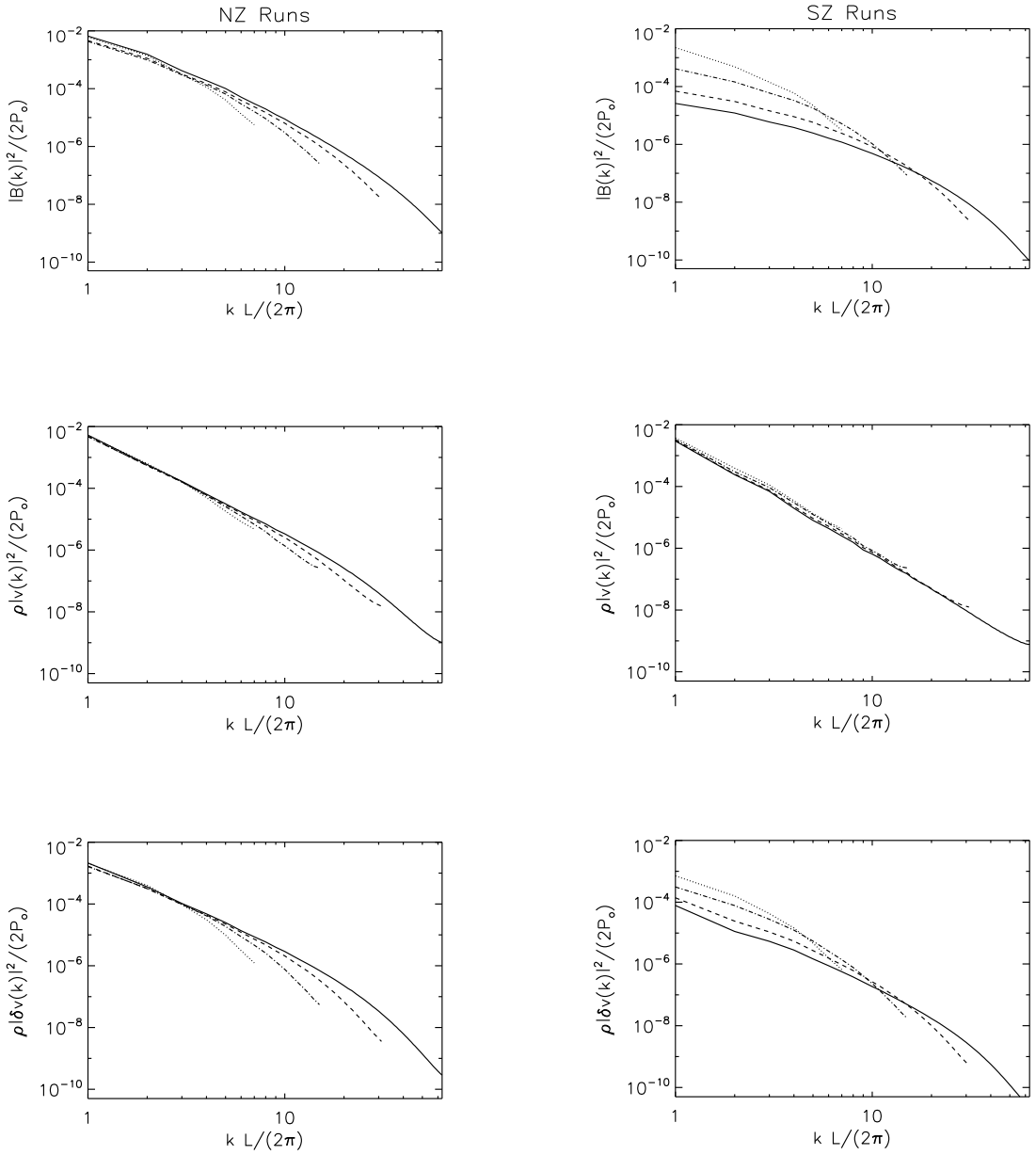

Fig. 5.— Spatial power spectra of various energy densities in the saturated state of the standard net flux (left panels) and zero net flux simulations (right panels). The spectra were obtained via an average over 161 frames in the saturated state and an average over shells of constant modulus $|\boldsymbol{k}|$. In each column, the first plot shows magnetic energy density, the second shows kinetic energy density, and the third shows perturbed kinetic energy density (as defined in the text). The effect of resolution is shown in each individual plot; the dotted line corresponds to the resolution with $N_x = 16$, the dot-dashed line corresponds to $N_x = 32$, the dashed line corresponds to $N_x = 64$, and the solid line corresponds to $N_x = 128$. All energy densities have been normalized to the initial gas pressure and are plotted against a dimensionless wave number (L is the length of the smallest dimension of the box).

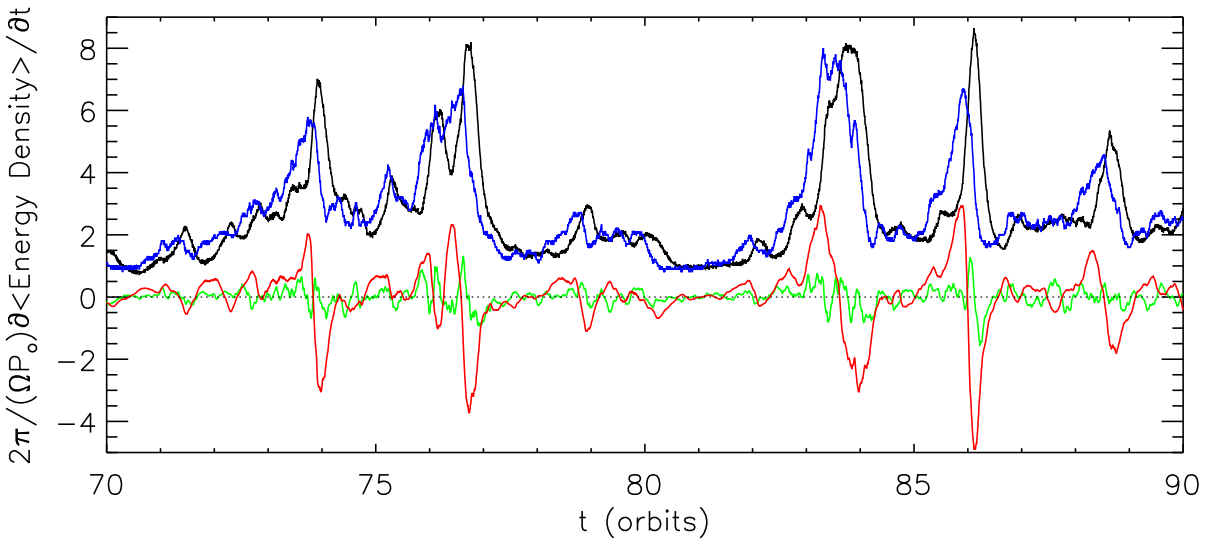

Fig. 6.— Time derivative of various volume-averaged energy densities for a 20 orbit period in the NZ128 simulation. The time derivative of the energy densities have been multiplied by an orbital time over the initial gas pressure. The dark blue line is the energy injection rate, $E_{\rm in}$, the black line is the thermal energy density derivative, $\dot{T}$, the green line is the kinetic energy density derivative, $\dot{K}$, and the red line is the magnetic energy density derivative, $\dot{M}$. The dotted line indicates zero.

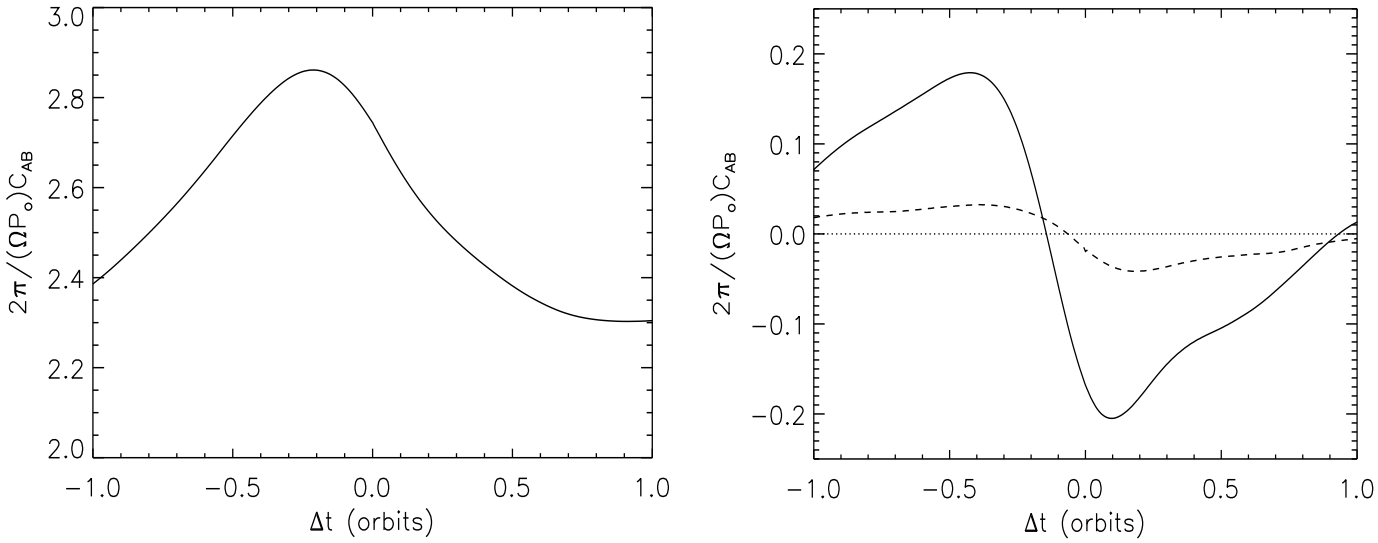

Fig. 7.— Correlation coefficients calculated over orbits 20 to 100 in the NZ128 simulation. The plot on the left was calculated by correlating the energy injection rate, $E_{\rm in}$, against the thermal energy time derivative, $\dot{T}$. The x-axis is the correlation length in time, and the y-axis is the coefficient multiplied by an orbital period over the initial gas pressure. The plot on the right was calculated by correlating the magnetic energy derivative, $\dot{M}$, (solid line) and kinetic energy derivative, $\dot{K}$, (dashed line) against the thermal energy derivative. The dotted line indicates $C_{AB} = 0$. Note that the two plots have different y scales.

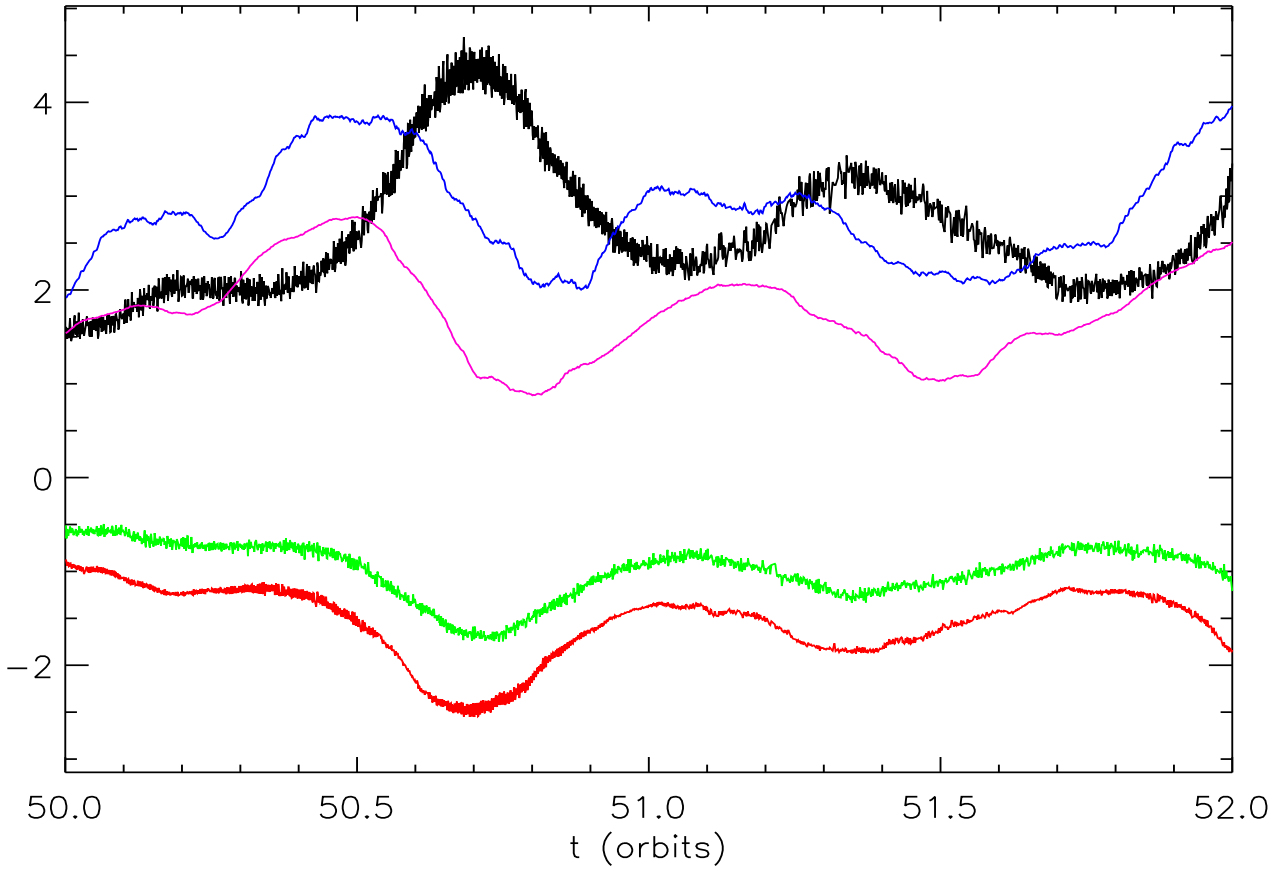

Fig. 8.— Various terms in the volume-averaged magnetic, kinetic, and thermal energy density evolution equations over a two orbit period of NZ128. The energy terms are $\dot{T}$ (black), $E_{\rm in}$ (blue), -$\dot{Q}_{\rm k}$ (green), -$\dot{Q}_{\rm m}$ (red), and the volume-averaged transfer rate from kinetic to magnetic energy (pink). All of these terms are defined in the text and have been multiplied by an orbital period over the initial gas pressure.

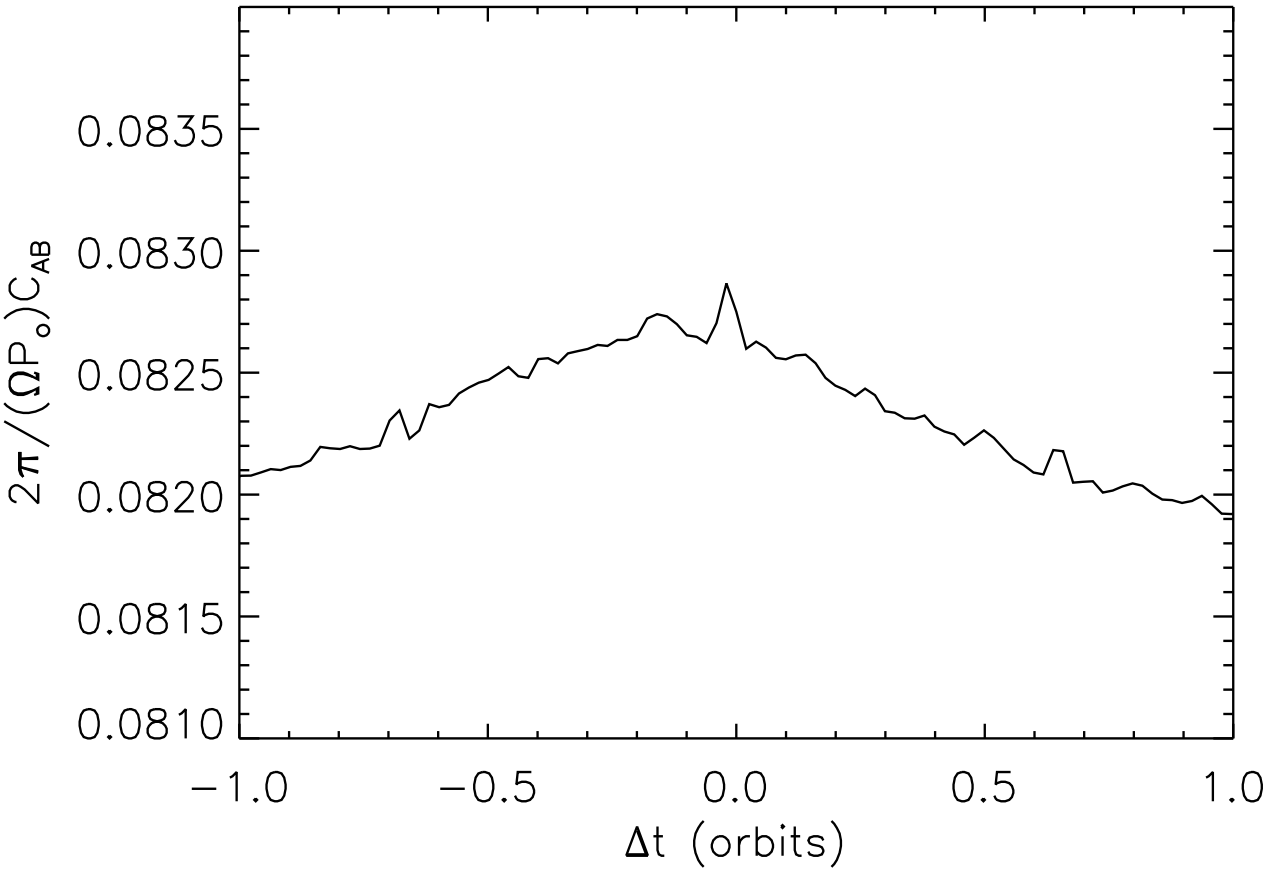

Fig. 9.— Correlation coefficient calculated over the saturated state of the SZ128 simulation. The coefficient was calculated by correlating the energy injection rate against the thermal energy density derivative. The x-axis is the correlation length in time, and the y-axis is the coefficient multiplied by an orbital period over the initial gas pressure. The narrow peaks in the curve correspond to residual effects from rebinning the energy derivatives (described in the text). The broader peak in the correlation function occurs at $\Delta t \sim$ -0.2 orbits.

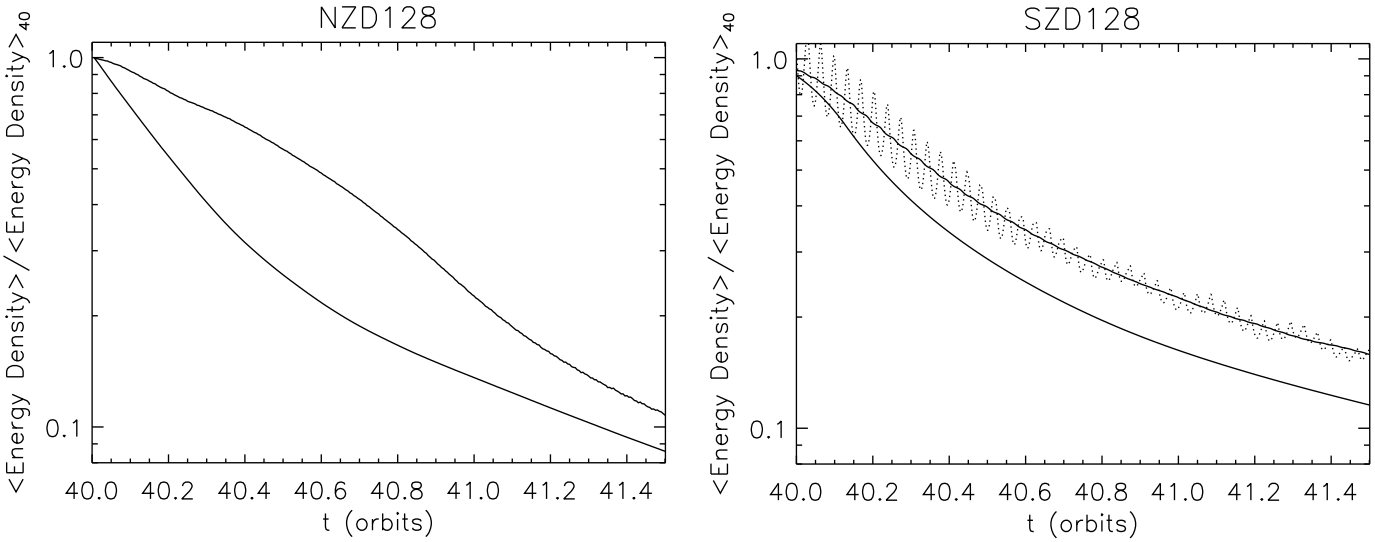

Fig. 10.— Volume-averaged magnetic and kinetic energy densities in the first 1.5 orbits of NZD128 (left) and SZD128 (right). In both plots, the upper curves correspond to the kinetic energy density and the lower curves correspond to the magnetic energy density. In SZD128, high frequency oscillations appear in the kinetic energy evolution. To smooth away these oscillations, a moving window average was applied to the kinetic energy density. The unsmoothed kinetic energy is shown by the dotted line, while the smoothed kinetic energy is the solid line. The magnetic energy density in the SZD128 plot has also been smoothed for consistency. Both the kinetic and magnetic energy densities have been normalized to their respective (unsmoothed) values at $t = 40$ orbits.

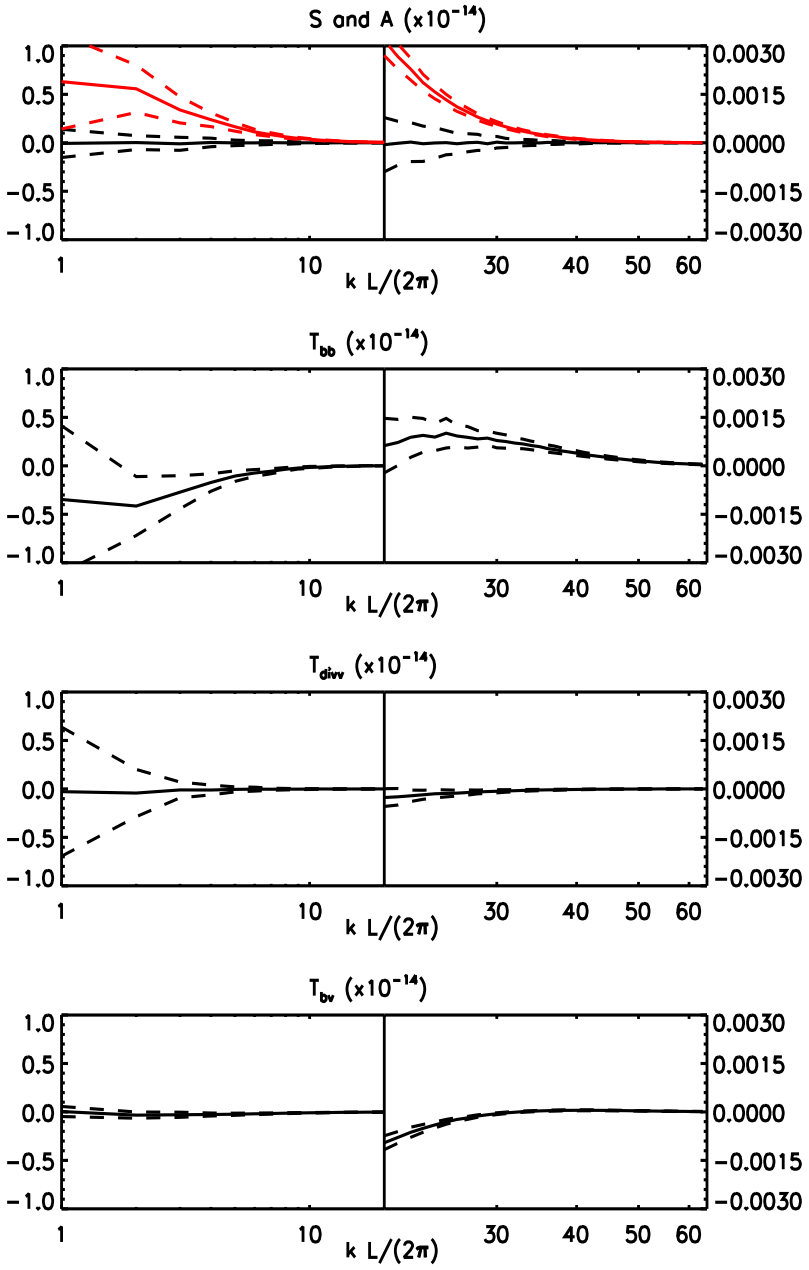

Fig. 11.— Magnetic Fourier transfer functions versus a dimensionless wave number (L is the length of the smallest dimension in the box) for SZ128. Each plot is displayed in two components; the left part shows the data for $1 < kL/(2\pi) < 20$, and the right part shows the data for $20 < kL/(2\pi) < 64$ by changing the x and y axis scaling. In all plots, the solid line is the average value for the transfer function. This average was obtained over 161 frames in the saturated state and shells of constant $|\boldsymbol{k}|$. The upper (lower) dashed line that matches color with the solid line correspond to the transfer function plus (minus) one temporal standard deviation. From top to bottom, the plots show S (red) and A (black), T_{bb}, $T_{\mathrm{div}v}$, and T_{bv}.

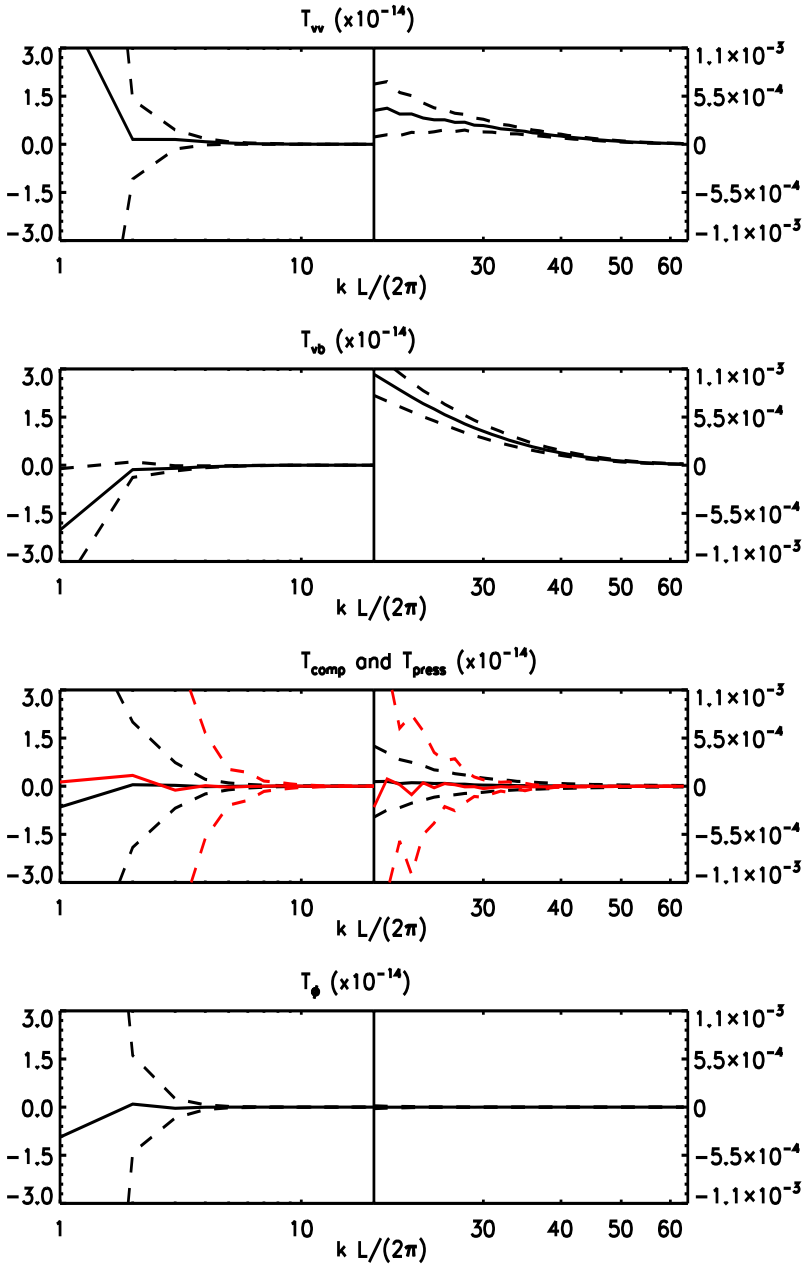

Fig. 12.— Kinetic Fourier transfer functions versus a dimensionless wave number (L is the length of the smallest dimension in the box) for SZ128. Each plot is displayed in two components; the left part shows the data for $1 < kL/(2\pi) < 20$, and the right part shows the data for $20 < kL/(2\pi) < 64$ by changing the x and y axis scaling. In all plots, the solid line is the average value for the transfer function. This average was obtained over 161 frames in the saturated state and shells of constant $|\boldsymbol{k}|$. The upper (lower) dashed line that matches color with the solid line correspond to the transfer function plus (minus) one temporal standard deviation. From top to bottom, the plots show T_{vv}, T_{vb}, $T_{\rm press}$ (red) and $T_{\rm comp}$ (black), and T_{ϕ}.

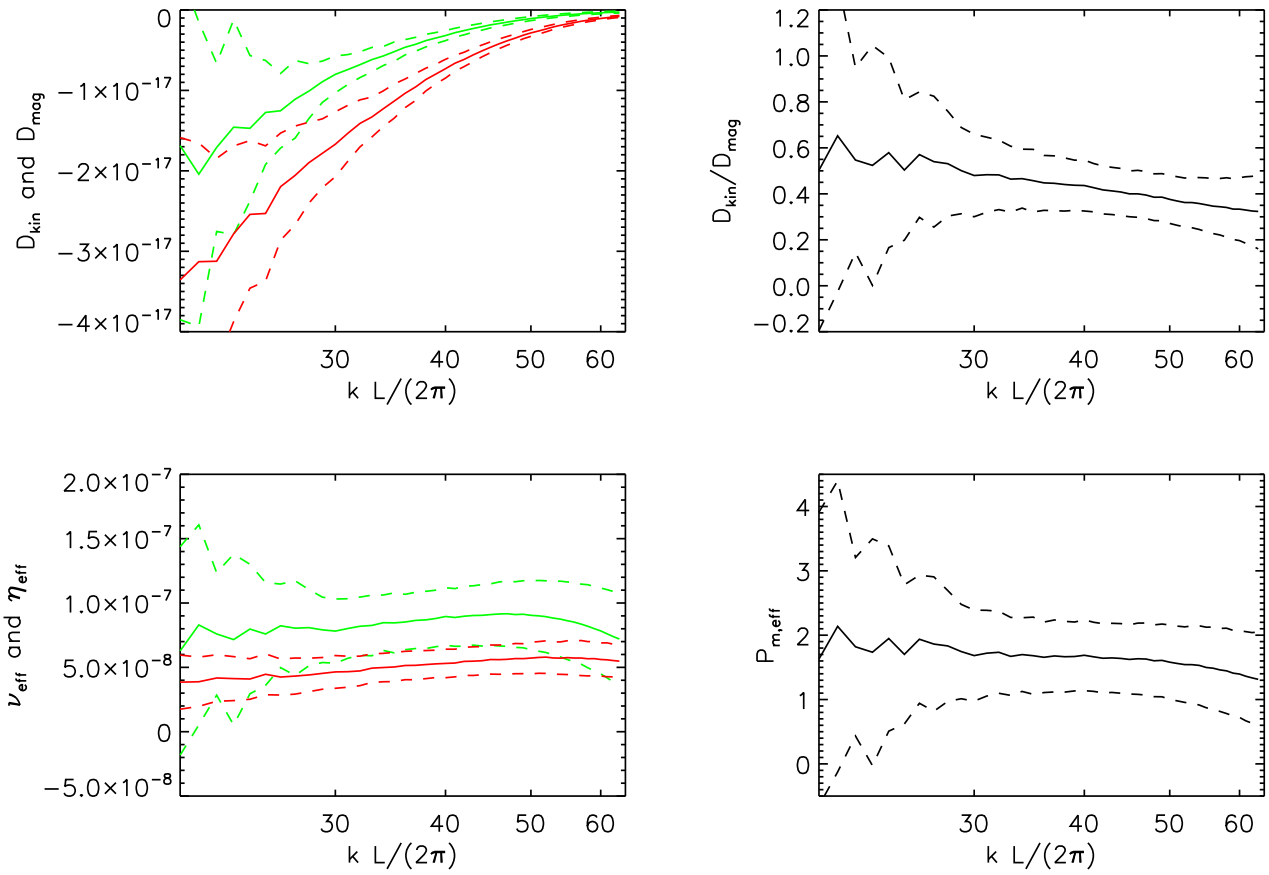

Fig. 13.— Numerical dissipation quantities plotted against a dimensionless wave number (L is the length of the smallest dimension in the box). These plots correspond to data from SZ128. The upper left plot shows the dissipation rate of kinetic energy (green) and magnetic energy (red) in Fourier space. The upper right plot shows the ratio of these two dissipation rates. The lower left plot shows the effective numerical viscosity (green) and resistivity (red). The lower right plot shows the ratio of the viscosity to resistivity (i.e., the effective Prandtl number). In all plots, the solid line is the average value for the quantity of interest. For $D_{\rm kin}$ and $D_{\rm mag}$, this average was obtained from averaging over shells of constant $|\boldsymbol{k}|$ and over 161 frames in the saturated state. The averaged viscosity and resistivity values were calculated as described in the text. The upper and lower dashed lines correspond to the error propagated from one temporal standard deviation.

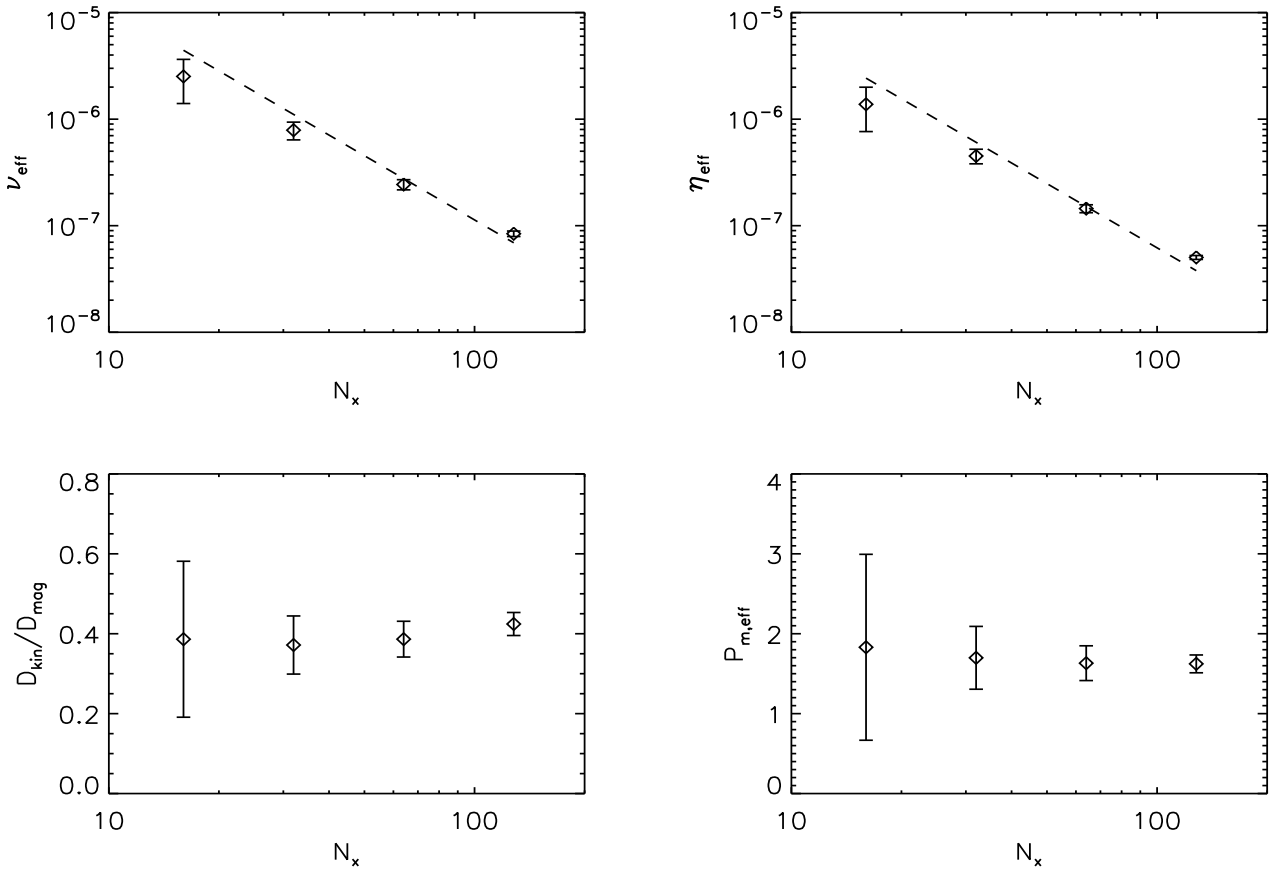

Fig. 14.— Averaged dissipation related quantities as a function of grid resolution. These plots correspond to data from the zero net flux simulations, SZ16, SZ32, SZ64, and SZ128. The upper left plot shows the effective viscosity versus x resolution. The dashed line shows $\nu_{\rm eff} \propto N_x^{-2}$. The upper right plot shows the effective resistivity versus x resolution. Again, the dashed line shows $\eta_{\rm eff} \propto N_x^{-2}$. The lower left plot shows the ratio of kinetic to magnetic dissipation versus x resolution. The lower right plot shows the effective Prandtl number versus x resolution. For each resolution, the data point was obtained from averaging the quantity as a function of k over values of k where the error in this quantity is not much larger than the mean value. The error bars represent the propagated errors from the temporal statistics.

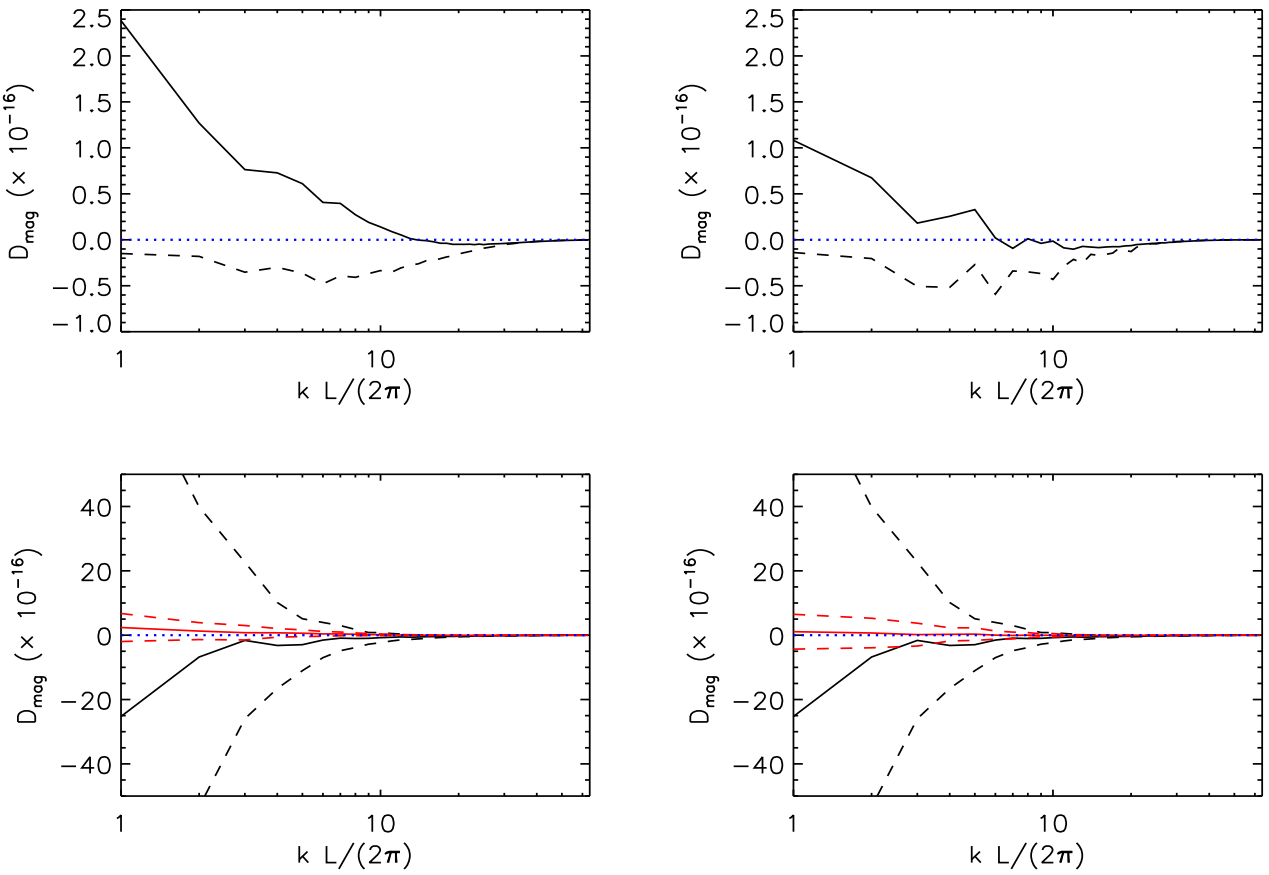

Fig. 15.— Magnetic dissipation rate from the SZ128 simulation for three versions of the transfer function analysis. The upper left plot and the red lines in the lower left plot correspond to the analysis in which $B_y = 0$ was assumed. The upper right plot and the red lines in the lower right plot correspond to the analysis in which both $B_y = 0$ and $k_y = 0$ were assumed. The black lines in the lower plots result from relaxing both of these assumptions. The solid lines in the upper plots correspond to $D_{\rm mag}$ whereas the dashed lines correspond to ηT_η with $\eta = 10^{-7}$ chosen to provide a reasonable match to $D_{\rm mag}$ at large k. The dashed lines in the lower plots correspond to one standard deviation above and below the quantity represented by the solid line of the same color. A horizontal line at zero is shown in all plots as the blue dotted line. Note the difference in y-axis scale between the upper and lower plots.

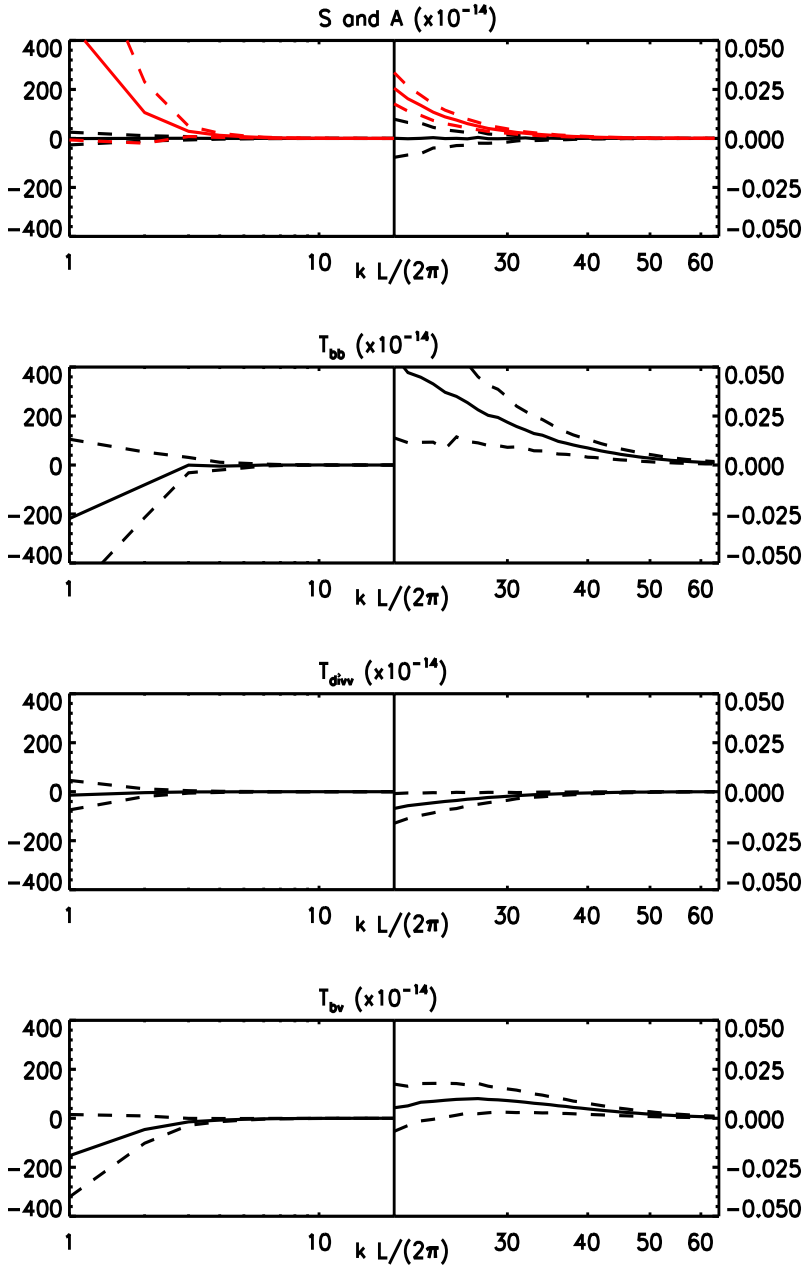

Fig. 16.— Magnetic Fourier transfer functions versus a dimensionless wave number (L is the length of the smallest dimension in the box) for NZ128. Each plot is displayed in two components; the left part shows the data for $1 < kL/(2\pi) < 20$, and the right part shows the data for $20 < kL/(2\pi) < 64$ by changing the x and y axis scaling. In all plots, the solid line is the average value for the transfer function. This average was obtained over 161 frames in the saturated state and shells of constant $|\boldsymbol{k}|$. The upper (lower) dashed line that matches color with the solid line correspond to the transfer function plus (minus) one temporal standard deviation. From top to bottom, the plots show S (red) and A (black), T_{bb}, $T_{\mathrm{div}v}$, and T_{bv}.

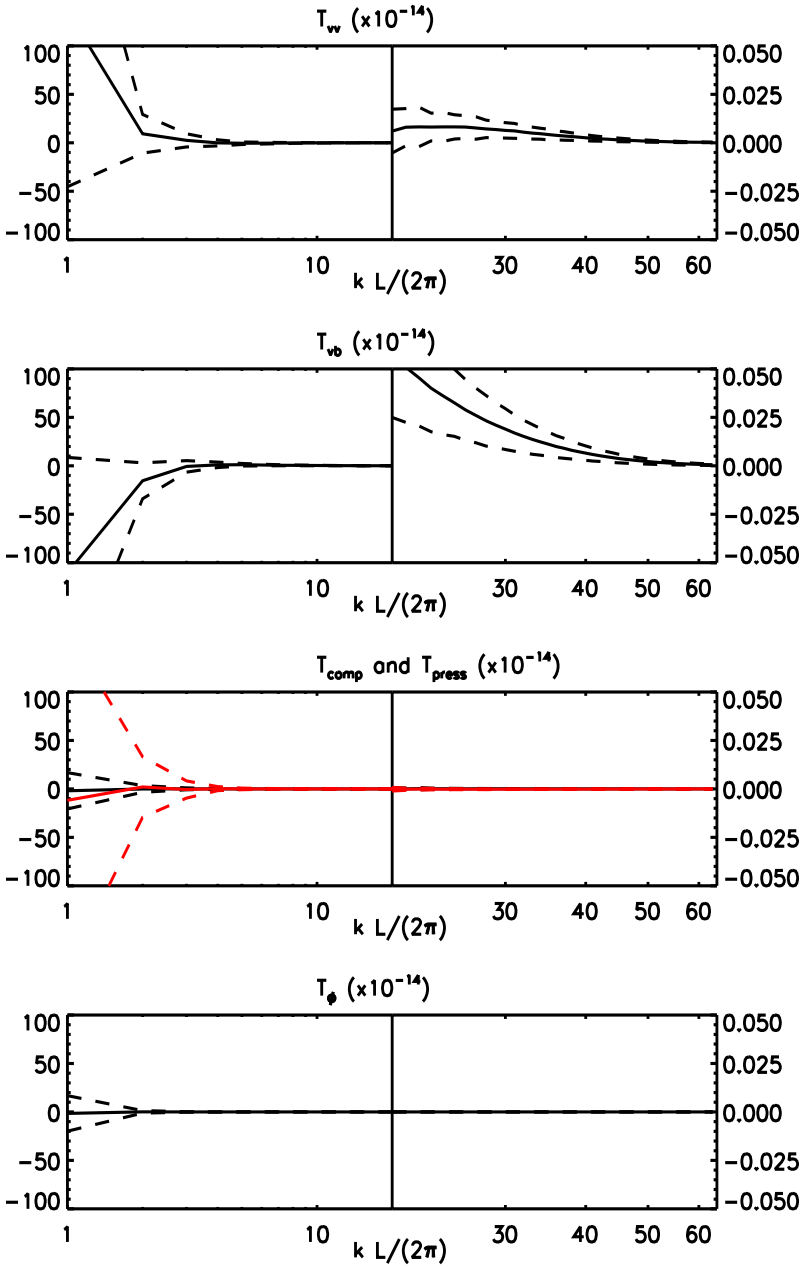

Fig. 17.— Kinetic Fourier transfer functions versus a dimensionless wave number (L is the length of the smallest dimension in the box) for NZ128. Each plot is displayed in two components; the left part shows the data for $1 < kL/(2\pi) < 20$, and the right part shows the data for $20 < kL/(2\pi) < 64$ by changing the x and y axis scaling. In all plots, the solid line is the average value for the transfer function. This average was obtained over 161 frames in the saturated state and shells of constant $|\boldsymbol{k}|$. The upper (lower) dashed line that matches color with the solid line correspond to the transfer function plus (minus) one temporal standard deviation. From top to bottom, the plots show T_{vv}, T_{vb}, $T_{\rm press}$ (red) and $T_{\rm comp}$ (black), and T_{ϕ}.

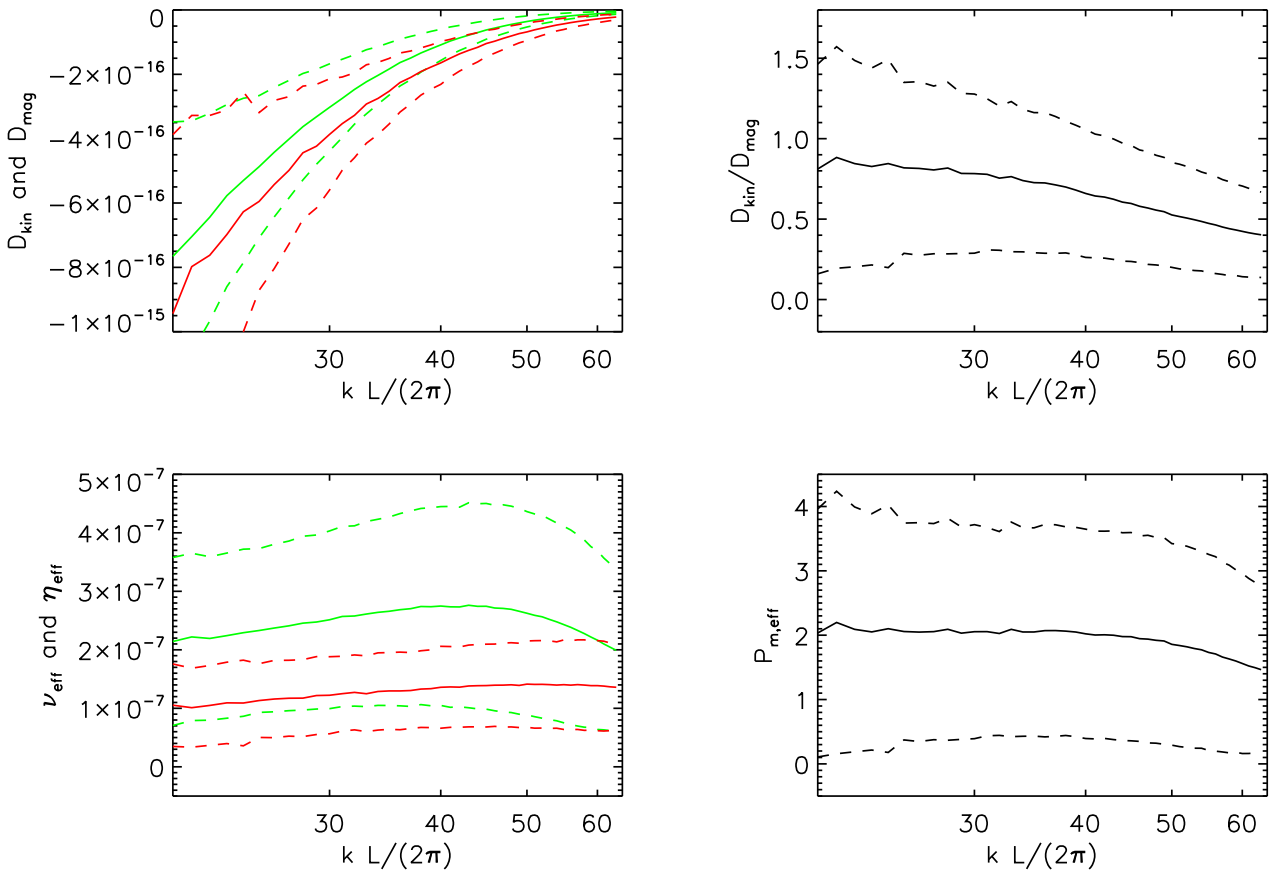

Fig. 18.— Numerical dissipation quantities plotted against a dimensionless wave number (L is the length of the smallest dimension in the box). These plots correspond to data from NZ128. The upper left plot shows the dissipation rate of kinetic energy (green) and magnetic energy (red) in Fourier space. The upper right plot shows the ratio of these two dissipation rates. The lower left plot shows the effective numerical viscosity (green) and resistivity (red). The lower right plot shows the ratio of the viscosity to resistivity (i.e., the effective Prandtl number). In all plots, the solid line is the average value for the quantity of interest. For $D_{\rm kin}$ and $D_{\rm mag}$, this average was obtained from averaging over shells of constant $|\boldsymbol{k}|$ and over 161 frames in the saturated state. The averaged viscosity and resistivity values were calculated as described in the text. The upper and lower dashed lines correspond to the error propagated from one temporal standard deviation.

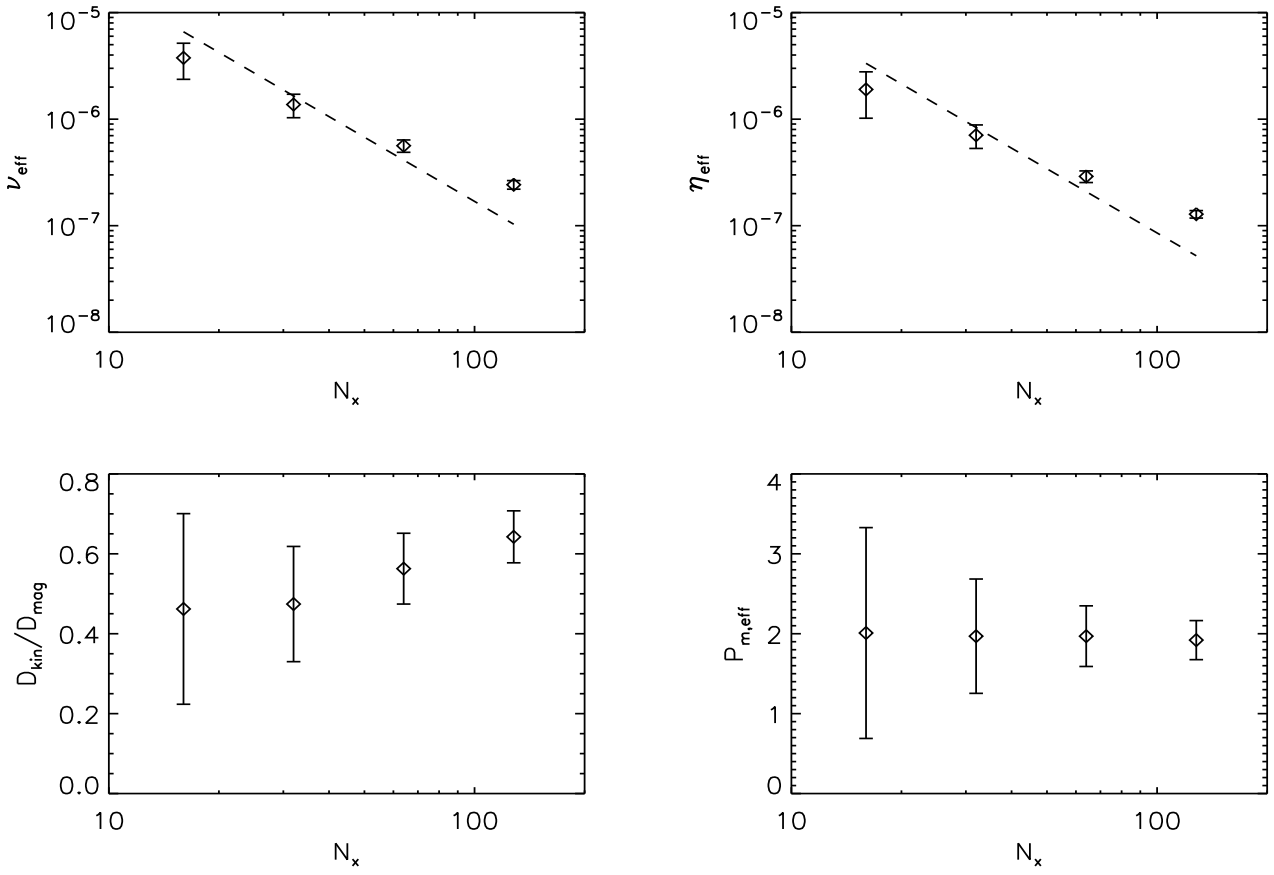

Fig. 19.— Averaged dissipation related quantities as a function of grid resolution. These plots correspond to data from the net flux simulations, NZ16, NZ32, NZ64, and NZ128. The upper left plot shows the effective viscosity versus x resolution. The dashed line shows $\nu_{\rm eff} \propto N_x^{-2}$. The upper right plot shows the effective resistivity versus x resolution. Again, the dashed line shows $\eta_{\rm eff} \propto N_x^{-2}$. The lower left plot shows the ratio of kinetic to magnetic dissipation versus x resolution. The lower right plot shows the effective Prandtl number versus x resolution. For each resolution, the data point was obtained from averaging the quantity as a function of k over values of k where the error in this quantity is not much larger than the mean value. The error bars represent the propagated errors from the temporal statistics.